JOURNAL OF GEOPHYSICAL RESEARCH, VOL. 112, D09202, doi:10.1029/2006JD007712, 2007

Have Australian rainfall and cloudiness increased due to the remote effects of Asian anthropogenic aerosols?

Leon D. Rotstayn,[1] Wenju Cai,[1] Martin R. Dix,[1] Graham D. Farquhar,[2] Yan Feng,[3] Paul Ginoux,[4] Michael Herzog,[3] Akinori Ito,[3] Joyce E. Penner,[3] Michael L. Roderick,[2] and Minghuai Wang[3]

Received 29 June 2006; revised 20 September 2006; accepted 1 December 2006; published 2 May 2007.

[1] There is ample evidence that anthropogenic aerosols have important effects on climate in the Northern Hemisphere but little such evidence in the Southern Hemisphere. Observations of Australian rainfall and cloudiness since 1950 show increases over much of the continent. We show that including anthropogenic aerosol changes in 20th century simulations of a global climate model gives increasing rainfall and cloudiness over Australia during 1951–1996, whereas omitting this forcing gives decreasing rainfall and cloudiness. The pattern of increasing rainfall when aerosols are included is strongest over northwestern Australia, in agreement with the observed trends. The strong impact of aerosols is primarily due to the massive Asian aerosol haze, as confirmed by a sensitivity test in which only Asian anthropogenic aerosols are included. The Asian haze alters the meridional temperature and pressure gradients over the tropical Indian Ocean, thereby increasing the tendency of monsoonal winds to flow toward Australia. Anthropogenic aerosols also make the simulated pattern of surface-temperature change in the tropical Pacific more like La Niña, since they induce a cooling of the surface waters in the extratropical North Pacific, which are then transported to the tropical eastern Pacific via the deep ocean. Transient climate model simulations forced only by increased greenhouse gases have generally not reproduced the observed rainfall increase over northwestern and central Australia. Our results suggest that a possible reason for this failure was the omission of forcing by Asian aerosols. Further research is essential to more accurately quantify the role of Asian aerosols in forcing Australian climate change.

Citation: Rotstayn, L. D., et al. (2007), Have Australian rainfall and cloudiness increased due to the remote effects of Asian anthropogenic aerosols?, *J. Geophys. Res.*, *112*, D09202, doi:10.1029/2006JD007712.

1. Introduction

[2] It has been understood for at least a decade that anthropogenic aerosols partly offset the warming effect of greenhouse gases and that inclusion of aerosols in climate models can improve the agreement between models and observations [*Mitchell et al.*, 1995]. More recently, results from several climate models have shown that spatially inhomogeneous aerosol forcing can alter atmospheric circulation and rainfall, especially at low latitudes. Aerosols cool the surface and (if absorbing aerosols are present) warm the lower atmosphere, stabilizing the boundary layer and suppressing convection in the most polluted regions [*Ramanathan et al.*, 2005]. In the tropics, this can result in increased (compensating) convection in other areas, which may be distant from the aerosol sources [*Rotstayn and Lohmann*, 2002a]. Possible impacts include summertime floods and droughts in China [*Menon et al.*, 2002b], droughts in the Sahel [*Rotstayn and Lohmann*, 2002a], and a weakening of the South Asian Monsoon [*Ramanathan et al.*, 2005]. Inclusion of aerosols in climate models has also been shown to lead to a decrease in modeled solar radiation at the Earth's surface [*Liepert et al.*, 2004; *Nazarenko and Menon*, 2005]. This helps to reconcile climate models with the observed downward trend in surface solar radiation that occurred from about 1960 to 1990, the so-called global dimming phenomenon [*Stanhill and Cohen*, 2001]. There is evidence of some reversal of global dimming since 1990 [*Wild et al.*, 2005], and this is broadly consistent with known aerosol reductions in many regions. If aerosols have contributed to global dimming, then aerosols are also likely to have contributed to observed

[1] Marine and Atmospheric Research, CSIRO, Aspendale, Victoria, Australia.
[2] CRC for Greenhouse Accounting, Research School of Biological Sciences, Australian National University, Canberra, ACT, Australia.
[3] Department of Atmospheric, Oceanic, and Space Sciences, University of Michigan, Ann Arbor, Michigan, USA.
[4] Geophysical Fluid Dynamics Laboratory, NOAA, Princeton, New Jersey, USA.

0148-0227/07/2006JD007712$09.00

decreases in pan evaporation [*Roderick and Farquhar*, 2002]. These and other studies show considerable evidence of aerosol effects on climate in the Northern Hemisphere (NH).

[3] In the relatively pristine Southern Hemisphere (SH), there is much less evidence of strong climatic effects due to aerosols, though observations over the Amazon basin do suggest the possibility of substantial effects there due to biomass-burning aerosols [*Hobbs et al.*, 1997; *Andreae et al.*, 2004; *Koren et al.*, 2004]. Australia is a continent with low levels of anthropogenic aerosols, which superficially suggests the absence of a substantial aerosol effect on Australian climate. However, several studies using atmospheric global climate models (GCMs) coupled to mixed-layer ocean models have shown an overall southward shift of tropical rainfall in response to anthropogenic aerosol forcing, which predominantly causes a cooling of the NH. Earlier studies considered only indirect aerosol effects [*Rotstayn et al.*, 2000b; *Williams et al.*, 2001; *Rotstayn and Lohmann*, 2002a], whereas more recent studies have considered direct and indirect aerosol effects [*Feichter et al.*, 2004; *Takemura et al.*, 2005; *Kristjánsson et al.*, 2005]. These results suggest the possibility of an impact on Australian climate from the large Asian aerosol haze.

[4] Averaged over Australia, observed climatic trends in the second half of the 20th century include increases in temperature [*Nicholls*, 2003; *Karoly and Braganza*, 2005], rainfall [*Smith*, 2004] and cloudiness [*Jones and Henderson-Sellers*, 1992] and decreases in diurnal temperature range (DTR) [*Karoly and Braganza*, 2005]. The rainfall trends since midcentury are dominated by increases over the northwestern and central parts of the continent, where they were found to be statistically significant [*Smith*, 2004], but there are decreasing trends over the northeast and south. Although the cloud observations are considered uncertain [*Jones and Henderson-Sellers*, 1992], increasing cloudiness is broadly consistent with increasing rainfall. Also, Australian interannual DTR changes have been found to correlate very strongly ($R = 0.90$) with changes in cloudiness [*Dai et al.*, 1997], so the decreasing DTR trend provides independent confirmation of the increasing cloudiness trend. Although aerosol increases can also contribute to decreases in DTR [*Hansen et al.*, 1995; *Nazarenko and Menon*, 2005], low aerosol levels over Australia probably explain why the correlation between DTR and cloudiness was found to be stronger over Australia than elsewhere by *Dai et al.* [1997]. Relatively low aerosol levels also make it difficult to attribute observed decreases in Australian pan evaporation [*Roderick and Farquhar*, 2004] to local aerosol increases.

[5] In this study we use a GCM to investigate the possibility that anthropogenic aerosol forcing has contributed to recent trends in the Australian hydrological cycle. We focus especially on rainfall trends, since rainfall fluctuations have large socioeconomic impacts over Australia, and high-quality rainfall observations are available. An important feature of Australian rainfall is its strong interannual variability. This variability is modulated, at least in part, by natural oscillations in the ocean basins to the east, south, and west of Australia. The influence of the El Niño Southern Oscillation (ENSO) has been known for many years, with El Niño (La Niña) events associated with low (high) rainfall over most of eastern Australia [e.g., *McBride and Nicholls*, 1983; *Ropelewski and Halpert*, 1987]. The connection between Indian Ocean SSTs and Australian rainfall variations was pointed out by *Nicholls* [1989]. Much recent research has focused on a natural mode referred to as the Indian Ocean Dipole [*Saji et al.*, 1999] and its link to Australian wintertime rainfall variations in a broad band stretching from the northwest to the southeast of the continent [e.g., *Ashok et al.* 2003]. To the south, the Southern Annular Mode (also known as the Antarctic Oscillation) is the major mode of variability. It has been linked to interannual rainfall variations over southern Australia, both in the southwest [e.g., *Cai et al.*, 2003a] and the southeast [*Meneghini et al.*, 2007].

[6] It is increasingly recognized that anthropogenic climate change can occur via changes in these natural modes of the climate system [*Clarke et al.*, 2001]. For example, AOGCMs forced by increasing atmospheric CO_2 have simulated an El Niño-like warming pattern in the Pacific Ocean [e.g., *Meehl and Washington*, 1996; *Cai and Whetton*, 2000], which suggests the disturbing possibility that future average rainfall might be lower over eastern Australia. Also, a robust feature of the SH response of GCMs to an increase of greenhouse gases is a shift of the Southern Annular Mode towards its "positive" state, with decreased pressure over Antarctica and increased pressure over the SH midlatitudes [*Cubasch et al.*, 2001; *Cai et al.*, 2003a]. This is also consistent with the study of *Yin* [2005], who found a poleward shift of the midlatitude storm tracks in 21st century simulations of 15 current climate models. Changes in the Southern Annular Mode have been observed, with a significant positive trend since the mid-1960s [*Thompson and Solomon*, 2002]. This is consistent with the sign of the response of GCMs to increasing greenhouse gases, although Antarctic ozone depletion has also been implicated [*Thompson and Solomon*, 2002]. Recent modeling has attributed the trend in the Southern Annular Mode to a combination of increasing greenhouse gases and ozone depletion [*Arblaster and Meehl*, 2006]. These findings suggest possible anthropogenic causes for observed Australian rainfall trends (which are considered further in section 3.2). A more general conclusion from this brief overview of Australian climate variability is that in the present study, we are attempting to attribute multidecadal trends that exist against a background of strong interannual variability.

[7] We have used a coupled ocean-atmosphere GCM (OAGCM) with an interactive aerosol scheme to perform climate simulations for the period 1871 to 2000. We performed an ensemble of eight runs with "all forcings" (greenhouse gases, ozone, aerosols, volcanic eruptions, and solar variations) and a further ensemble of eight runs that only differed from the "all forcing" runs in that the emissions of anthropogenic aerosols and their precursors were held at their 1870 levels. The differences between the two ensembles were used to deduce the effects of anthropogenic aerosols. The paper is organized as follows. The model and experiments are described in section 2. Modeled and observed trends in the Australian hydrological cycle during 1951–1996 are presented in section 3, and dynamical aspects of the simulations are considered in section 4. A sensitivity test designed to isolate the effects

Table 1. Efficiencies Assumed for In-Cloud and Below-Cloud Scavenging of Aerosol Mass by Liquid and Frozen Precipitation

	Liquid In-Cloud	Liquid Below-Cloud	Frozen In-Cloud	Frozen Below-Cloud
Sulfate	0.6	0.05	0	0.01
POM hydrophobic	0	0.05	0.1	0.01
POM hydrophilic	0.6	0.05	0	0.01
BC hydrophobic	0	0.05	0.1	0.01
BC hydrophilic	0.6	0.05	0	0.01
Dust 0.1–1 μm	0.1	0.05	0.1	0.01
Dust 1–2 μm	0.1	0.1	0.1	0.02
Dust 2–3 μm	0.1	0.2	0.1	0.04
Dust 3–6 μm	0.1	0.5	0.1	0.1

of Asian anthropogenic aerosols is presented in section 5. Further discussion is in section 6, and conclusions are in section 7.

2. Model and Experiments

2.1. Atmospheric Model

[8] The atmospheric model used in this study is a low-resolution (spectral R21) version of the Mk3 CSIRO atmospheric GCM. The R21 model has 18 hybrid vertical levels and a horizontal resolution of approximately 5.6° in longitude and 3.2° in latitude. A standard high-resolution version of the Mk3 model has been described in detail by *Gordon et al.* [2002]. However, the standard version did not include an interactive aerosol scheme and used an older radiation scheme that did not treat aerosol scattering or absorption. Since then, a comprehensive treatment of the tropospheric sulfur cycle was included in the CSIRO GCM [*Rotstayn and Lohmann*, 2002b] and treatments of other aerosol components, based on established schemes from other models, were subsequently added. Here, we summarize the aerosol schemes, the treatment of aerosol-cloud interactions, the features of an updated radiation code, and the treatment of aerosol optical properties in the new (Mk3A) model.

[9] Transport of aerosols and other trace quantities occurs by advection, vertical turbulent mixing, and vertical transport inside deep convective clouds [*Rotstayn and Lohmann*, 2002b]. Vertical advection is handled using a flux-corrected transport scheme [*Van Leer*, 1977], and horizontal advection is handled via a semi-Lagrangian scheme [*McGregor*, 1993]. The treatment of vertical turbulent mixing is based on stability-dependent K-theory [*Louis*, 1979]. Under convective conditions, an additional nonlocal counter-gradient flux is added [*Holtslag and Boville*, 1993]. Convective transport is based on the vertical profiles of the updraft mass flux and compensating subsidence generated by the convection scheme [*Gregory and Rowntree*, 1990].

[10] Prognostic variables in the sulfur-cycle model are dimethyl sulfide (DMS), sulfur dioxide (SO_2), and sulfate. The treatment of the sulfur chemistry is based on that in ECHAM4 [*Feichter et al.*, 1996]. The carbonaceous aerosol module [*Cooke et al.*, 1999] assumes an e-folding time of 1.15 days for the conversion of black carbon (BC) and particulate organic matter (POM) from their hydrophobic to hydrophilic forms. The treatment of mineral dust emission [*Ginoux et al.*, 2004] is based on satellite analyses that identified major dust sources as topographic depressions in which a sufficiently deep layer of alluvium was able to accumulate [*Prospero et al.*, 2002]. Four size bins are used for prognostic dust, with radii ranging from 0.1 to 1, 1 to 2, 2 to 3, and 3 to 6 μm, respectively. Two modes of sea salt aerosol (film-drop and jet-drop) are diagnosed at each time step as a function of 10-m wind speed above the ocean surface [*O'Dowd et al.*, 1997], but they are not prognostic variables, in the sense that they are not transported by the model. Sea salt aerosol is assumed to be well mixed in the marine boundary layer and is set to zero above the top of the boundary layer. This simple approach is similar to that used in the Met Office's Unified Model [*Jones et al.*, 2001].

[11] Large-scale wet scavenging processes are linked to the warm rain and frozen precipitation processes in the stratiform cloud microphysical scheme [*Rotstayn*, 1997; *Rotstayn et al.*, 2000a] and the convection scheme [*Gregory and Rowntree*, 1990]. Below-cloud scavenging is assumed proportional to the area swept out by precipitation, based on the negative-exponential raindrop or snowflake size distribution, with a constant of proportionality (collection efficiency) as defined in Table 1. In-cloud scavenging is proportional to the amount of precipitation removed, divided by the liquid water (or ice water) content, with a constant of proportionality (scavenging efficiency) as defined in Table 1. Many of the numbers in Table 1 are highly uncertain, especially where frozen precipitation is concerned. Also included in the scheme is reevaporation of aerosol due to evaporation of rain (or snow), as described previously [*Rotstayn and Lohmann*, 2002b]. These treatments apply to sulfate, POM, BC, and dust (but not sea salt, since it is not a prognostic variable).

[12] The shortwave radiation scheme is a two-stream code with 12 bands [*Grant and Grossman*, 1998; *Grant et al.*, 1999]. The aerosol species treated are tropospheric sulfate, BC, POM, dust, sea salt, and stratospheric aerosol from volcanic eruptions. Except for carbonaceous aerosol (which is assumed to be an internal mixture of BC and POM), all the aerosol components are treated as external mixtures. The optical properties of sulfate, sea salt, and hydrophilic POM and BC account for hygroscopic aerosol growth, based on Kohler theory. Details of the assumed size distributions, optical properties and hygroscopic growth of tropospheric aerosol are given in Table 2. Owing to the computational expense of the calculation of the dependence of aerosol single-scattering properties on relative humidity (and BC fraction for carbonaceous aerosol) in the aerosol optical property routine [*Grant et al.*, 1999], we implemented these via lookup tables. Mie calculations were performed to generate tables of aerosol specific extinction, single-scattering albedo (SSA) and asymmetry parameter in each shortwave band, at 21 relative humidities ranging from 0 to 99% (in increments of 5% from 0 to 95%). For carbonaceous aerosol, these tables were generated for 16 equally spaced BC volume fractions ranging from 0 to 30%. In the GCM, linear interpolation in relative humidity (and BC volume fraction) was used to determine the single-scattering properties of each aerosol species. We enhanced the treatment of cloud-radiative effects in the shortwave scheme to include ice clouds [*Warren*, 1984; *Francis et al.*, 1994], which were approximated as water clouds in the original shortwave code. Also included is a simple treatment of the effect of BC on snow albedo [*Hansen and Nazarenko*,

Table 2. Size Distributions and Radiative Properties of Dry Tropospheric Aerosol

	Mode Radius, μm	Geometric Standard Deviation	Density, g cm^{-3}	Refractive Index at 550 nm
Sulfate[a]	0.05	1.9	1.77	$1.53 - 1.0 \times 10^{-7}i$ [*Toon et al.*, 1976]
POM + BC[b]	0.08	1.65	1.25 (mixture)	POM: $1.53 - 1.0 \times 10^{-7}i$ [*Toon et al.*, 1976]
			1.5 (BC)	BC: $1.80 - 0.50i$ [*Twitty and Weinman*, 1971]
Small dust[c]	0.01	1.4	2.4	$1.53 - 5.5 \times 10^{-3}i$ [*d'Almeida et al.*, 1991][d]
	0.045	1.6	2.4	As above
Large dust[c]	0.275	2.5	2.4	As above
Small sea salt[e]	0.035	1.92	2.165	$1.50 - 1.0 \times 10^{-8}i$ [*Shettle and Fenn*, 1979]
Large sea salt[e]	0.35	1.7	2.165	As above

[a]The size distribution for tropospheric sulfate is the fossil-fuel size distribution from *Penner et al.* [2001, Table 5.1]. It is assumed to have the optical properties and hygroscopic growth behavior of ammonium sulfate.

[b]The size distribution for the internal mixture of POM and BC is the biomass-burning size distribution from *Penner et al.* [2001, Table 5.1], with density 1.25 g cm^{-3}. The model's hydrophilic POM and BC is assumed to consist of 30% soluble material with the hygroscopic growth behavior of ammonium sulfate. The model's hydrophobic POM and BC is assumed to be completely nonhygroscopic.

[c]The dust size distribution is a superposition of three modes based on observations over the Atlantic Ocean [*de Reus et al.*, 2000]; small dust (the first model size bin with $r < 1$ μm) consists of the two modes shown with number fractions 0.198 and 0.802, respectively. Large dust (three model size bins with $r \geq 1$ μm) consists of one lognormal mode.

[d]We used the refractive indices from *d'Almeida et al.* [1991] to calculate the wavelength-dependent extinction, single scattering albedo (SSA), and asymmetry factor, and then scaled the SSAs to give SSA of 0.98 at 670 nm, to be consistent with the value used by *Bellouin et al.* [2003].

[e]The size distributions for sea salt are based on measurements taken over the Pacific Ocean by *Quinn et al.* [1996]. The number concentrations of small sea salt and large sea salt are those of the film-drop and jet-drop modes, respectively, from the windspeed-dependent parameterization of *O'Dowd et al.* [1997]. The treatment of hygroscopic growth follows the Navy Aerosol Model [*Gerber*, 1985].

2004]. The longwave scheme [*Chou et al.*, 2001; *Chou and Lee*, 2005] has 10 bands. Unlike the longwave code in the standard Mk3 model, the scheme treats non-CO_2 greenhouse gases (methane, nitrous oxide, and halocarbons) and aerosols. At present, the only aerosol included in the longwave scheme (as well as the shortwave scheme) is stratospheric aerosol from volcanic eruptions, which is assumed to have the properties of ammonium sulfate [*Sato et al.*, 1993].

[13] Cloud droplet number concentrations (cm^{-3}) over oceans (N_{ocean}) and land (N_{land}) were estimated empirically by *Menon et al.* [2002a] as

$$N_{\text{ocean}} = 10^{2.41+0.50\log(\text{SO4})+0.13\log(\text{OM})+0.05\log(\text{SS})} \quad (1)$$

and

$$N_{\text{land}} = 10^{2.41+0.50\log(\text{SO4})+0.13\log(\text{OM})}, \quad (2)$$

where SO4, OM, and SS are the mass concentrations of sulfate, particulate organic matter, and sea salt, respectively, in μg m^{-3}. We use equation (1) over oceans but reduce the coefficient that multiplies SO4 in equation (2) from 0.50 to 0.26, which was the value obtained from extensive observations in an earlier study [*Boucher and Lohmann*, 1995]. The physical justification for this "tuning" is the higher level of background aerosol over land, which results in lower supersaturations and a weaker expected dependence of N on anthropogenic sulfate, as seen in the observational data [*Boucher and Lohmann*, 1995]. Equation (1) was based on data from only two field experiments, both in the eastern North Atlantic, and it is uncertain whether it is valid to extend it to large continental areas, so we reverted to the smaller coefficient from *Boucher and Lohmann* [1995] over land. Although there is evidence that dust particles can act as efficient cloud condensation nuclei when coated with a layer of sulfate or other soluble material [e.g., *Yin et al.*, 2002], we have not included mineral dust in the parameterization of cloud droplet number concentration because of the large uncertainties and because our model does not yet include interactions among different aerosol species.

[14] In stratiform clouds, the droplet number concentration determines both the first [*Twomey*, 1977] and second [*Albrecht*, 1989] indirect effects. The first indirect effect enters the model via the parameterization of droplet effective radius in the radiation scheme [*Rotstayn and Liu*, 2003]. The second indirect effect enters via the parameterization of autoconversion (coalescence of cloud droplets) in the cloud microphysical scheme [*Rotstayn and Liu*, 2005]. The treatments of both these effects account for the observed increase of droplet spectral dispersion with increasing droplet concentration [*Liu and Daum*, 2002]. The convection scheme only includes very simple microphysics [*Gregory and Rowntree*, 1990], so the second indirect effect of aerosols on convective clouds is omitted. However, the first indirect effect is included, following the same scheme as used for stratiform clouds.

2.2. Ocean and Sea-Ice Models

[15] The oceanic and sea-ice components of the model are based on those from the earlier Mk2 CSIRO climate model, since the Mk3 ocean model [*Gordon et al.*, 2002] is only configured for coupling to the higher-resolution (spectral T63) atmospheric model. The sea-ice model [*O'Farrell*, 1998] includes the cavitating fluid rheology of *Flato and Hibler* [1990] and the three-layer ice thermodynamics of *Semtner* [1976]. The oceanic component is based on the Cox-Bryan code [*Cox*, 1984] and has the same horizontal resolution as the atmospheric model, with 21 levels in the vertical. Oceanic tracers are advected by the resolved large-scale velocity field together with an eddy-induced transport velocity [*Gent et al.*, 1995]. The coupling of the atmospheric and oceanic model components is done using flux adjustments to mitigate spurious climate drift. The flux adjustments are fixed in time, so they are not expected to contribute to the climatic trends that we consider in this study. Further

Table 3. Global Anthropogenic Emissions of Aerosols and Aerosol Precursors for 1870 and 2000

		1870	2000
Sulfur (Tg S)	anthropogenic[a]	3.2	61.7
POM (Tg C)	total	14.3	58.9
	biomass burning[b]	13.7	34.6
	fossil fuel	0.1	2.2
	fossil fuel SOA[c]	0.5	22.1
BC (Tg C)	total	2.1	8.2
	biomass burning[b]	2.1	5.4
	fossil fuel	0.1	2.8

[a]Further details of the breakdown of anthropogenic sulfur emissions are given in Figure 2 of *Smith et al.* [2004].

[b]Biomass burning includes open-vegetation burning and biofuel use [*Ito and Penner*, 2005].

[c]SOA refers to the emission of fossil-fuel secondary organic aerosol implied by the scaling up of the fossil-fuel POM emissions described in the text.

details of the oceanic component and the coupling procedures have been given previously by *Gordon and O'Farrell* [1997] and *Hirst et al.* [2000].

2.3. Experimental Setup

[16] Each run covers the period 1871 to 2000 and uses an initial condition taken from a preindustrial control run that had been integrated for several hundred years to reach a state of approximate equilibrium. The initial conditions for the individual runs are separated by 20 years to ensure independence of the runs. Each of the eight runs in the "all forcing" (ALL) ensemble is forced by historical changes in long-lived greenhouse gases [*Hansen et al.*, 2002], ozone [*Kiehl et al.*, 1999], solar variations [*Lean and Rind*, 1998], volcanic sulfate (updated from *Sato et al.* [1993]), and anthropogenic emissions of aerosols and aerosol precursors (described below). Changes in land cover are not included. The setup of the eight runs in the "all except aerosols" (AXA) ensemble is identical to that of the ALL runs, except that anthropogenic emissions of aerosols and their precursors are held at 1870 levels throughout each run.

[17] Regarding aerosols, historical anthropogenic emissions are included for sulfur [*Smith et al.*, 2001, 2004] and carbonaceous aerosols [*Ito and Penner*, 2005]. As discussed by these authors, such historical estimates are highly uncertain. Ninety seven percent of the sulfur emissions are assumed to occur as sulfur dioxide, and the remaining 3% occur as primary sulfate aerosol. The carbonaceous aerosol emissions include primary sources of BC and POM from the burning of fossil fuel, open vegetation, and biofuel. Emissions of BC and POM from open vegetation and biofuel are assumed to be hydrophilic, while emissions from fossil fuel are assumed to be 50% hydrophilic and 50% hydrophobic. Since secondary sources of POM are not included in the inventory, we multiplied the fossil fuel POM source for each year by a constant factor of 11.2 so that the global emission for 1985 matched that from an earlier inventory for the mid-1980s [*Penner et al.*, 1993; *Liousse et al.*, 1996], which gave reasonable agreement with observations when used as the basis for a major model intercomparison [*Penner et al.*, 2001], as well as another recent modeling study [*Liu et al.*, 2005]. Scaling up the fossil fuel POM emissions is a simple way to allow for secondary sources of POM (see discussion below). Anthropogenic sources of sulfur, POM, and BC for the years 1870 and 2000 in our model are compared in Table 3, assuming a scale factor of 1.3 for conversion of organic carbon to POM. Note that even with the large scale-factor we applied to the fossil fuel POM emissions, our fossil fuel POM emissions for the year 2000 (24.3 Tg C) are within the range used in recent models (7.5 Tg C to 28.1 Tg C, according to *Liu et al.* [2005], who emphasized the uncertainty of the emissions of carbonaceous aerosols). Also, our total POM emissions for the year 2000 (75.3 Tg C, including natural sources) are close to the average (74.3 Tg C) from the AeroCom models considered by *Textor et al.* [2006].

[18] Global anthropogenic emissions of sulfur, BC and POM from 1871 to 2000 are shown in Figure 1a. Each species shows a relatively gradual rise until about 1950, followed by a more rapid increase as industrial development occurred after World War II. Global sulfur emissions peaked in the late 1970s and then started to fall, due to the introduction of emission controls. Global emissions of carbonaceous aerosols continued to increase until the late 1990s. There is also considerable geographical variation in the emission histories for these species [*Smith et al.*, 2001; *Ito and Penner*, 2005]. For example, since about 1980, there has been a strong shift of sulfur emissions away from Europe and North America and toward Asia. Figure 1b shows the variation with time of emissions from "Asia,"

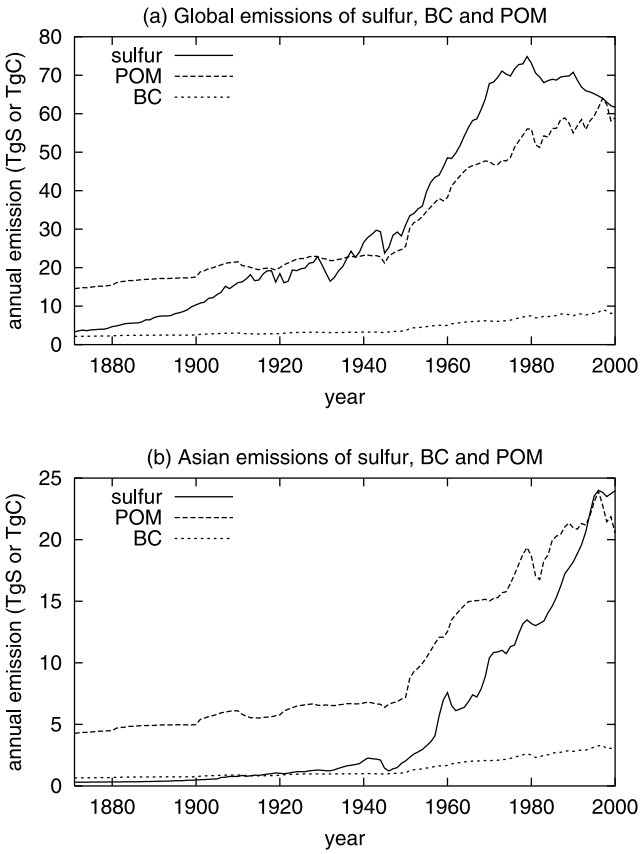

Figure 1. Time variation of (a) global and (b) Asian anthropogenic emissions of sulfur, POM, and BC. A factor of 1.3 is used in the model to convert from organic carbon to POM. See text for description of the region defined as "Asia."

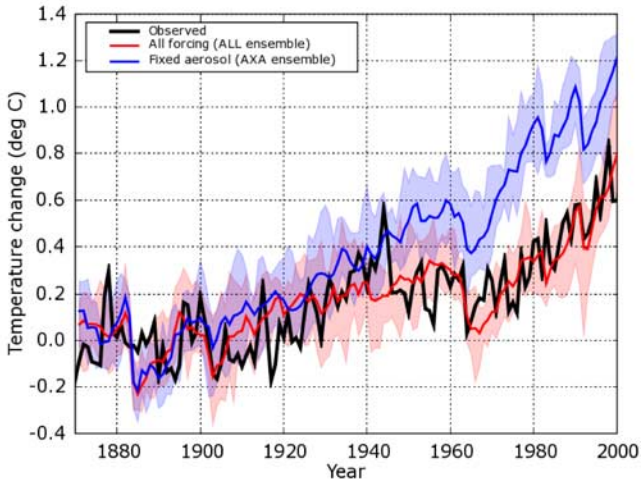

Figure 2. Time variation of global-mean T_s (relative to 1871–1900 mean) from the HadCRUT2 observations and from the ALL and AXA ensembles. Solid lines show the ensemble mean, and shading shows the range of individual runs within each ensemble. Each run uses its own 1871–1900 mean in the calculation of temperature change.

which we defined for the purpose of this study as a rectangular region from the equator to 45°N and from 70°E to 160°E (based on the hypothesis that NH aerosol sources from outside this region are too far away from Australia to substantially affect Australian climate). In contrast to the global emissions of sulfur, Asian emissions of sulfur, POM, and BC all continued to increase at least until the mid-1990s.

[19] The model also includes natural sources of sulfur [*Rotstayn and Lohmann*, 2002b]. These comprise SO_2 from noneruptive volcanoes, amounting to 8.0 Tg S yr^{-1} [*Spiro et al.*, 1992; *Graf et al.*, 1997], and biogenic emissions of DMS from oceans. The oceanic DMS source is calculated using the flux parameterization of *Nightingale et al.* [2000] and a global database of DMS measurements [*Kettle et al.*, 1999; *Kettle and Andreae*, 2000]. It amounts to 22.5 Tg S yr^{-1} in 1870 and 22.7 Tg S yr^{-1} in 2000. The small increase in the DMS source between 1870 and 2000 is mainly due to an increase in wind speed south of 50°S during the simulation (since temperature-related changes in oceanic DMS concentration are not included in the model). For natural organic carbon from terpenes [*Guenther et al.*, 1995], a yield of 13% is assumed for rapid conversion to POM, giving an annual source of 16.4 Tg C (21.3 Tg of POM using a conversion factor of 1.3).

[20] With this aerosol treatment, we estimate a change in top-of-atmosphere net downward irradiance of −1.1 W m^{-2} between 1870 and 1990 due to the combined direct and indirect aerosol effects. This figure was obtained from the difference of two 20-year runs with prescribed climatological sea surface temperatures (SSTs), with aerosol and aerosol-precursor emissions set to 1870 or 1990 levels, respectively, and other forcing factors held constant at late 20th century levels. This method (using the difference of two runs) is the usual approach when the second indirect effect is included, since it is difficult to estimate the second indirect effect without allowing the meteorology to evolve. The method was found to be satisfactory by *Rotstayn and Penner* [2001], even though feedbacks (such as changes in land-surface temperature) are allowed to occur. They referred to it as a "quasi forcing." A refinement of the method, designed to account for these feedbacks and hence provide a better predictor of the equilibrium global-mean temperature response to a given radiative perturbation, was suggested by *Hansen et al.* [2005], namely

$$F_s = F_o + \delta T_o/\lambda, \tag{3}$$

where F_o is the "quasi forcing" from above, δT_o is the global-mean surface temperature change when the radiative perturbation is introduced but the SSTs are held fixed, and λ is an estimate of the model's equilibrium climate sensitivity parameter (in K per W m^{-2}). *Hansen et al.* [2005] called F_s the "fixed SST forcing." From the last 10 years of our two 20-year runs, $\delta T_o = -0.072$ K, and for the CSIRO GCM $\lambda \approx 0.8$ K per W m^{-2} [*Rotstayn and Penner*, 2001]. Thus $F_s = -1.2$ W m^{-2} is a more accurate estimate of the net anthropogenic aerosol forcing in our model between 1870 and 1990. Of this, the direct aerosol forcing is −0.39 W m^{-2} (calculated by making a second call to the shortwave radiation scheme, with aerosols turned off, in both runs) and the remainder (−0.8 W m^{-2}) can be attributed to the indirect aerosol effect.

[21] Figure 2 shows the time evolution of global-mean near-surface temperature (T_s) changes from the HadCRUT2 observations [*Jones and Moberg*, 2003; *Rayner et al.*, 2003] and from the model runs. The ALL ensemble clearly gives a better simulation of the observed global-mean T_s changes, since the AXA ensemble overestimates the warming after about 1950. This result (that inclusion of aerosol forcing improves the simulation of global-mean T_s changes) has been seen before in other GCMs [e.g., *Mitchell et al.* 1995].

2.4. Overview of the Aerosol Treatment

2.4.1. Evaluation of the Simulation

[22] Since we are emphasizing aspects of the climatic response to aerosol forcing, which is highly uncertain, a brief evaluation of the aerosol simulation is included here. A detailed evaluation of the sulfur cycle component has been presented [*Rotstayn and Lohmann*, 2002b], but the other aerosol components in the CSIRO GCM have not yet been presented in the open literature (though they are mostly based on previously published schemes). Table 4 compares the global averages of dry aerosol column burden from the year 2000 of the ALL ensemble with the results from 16 models that participated in the AeroCom intercomparison [*Kinne et al.*, 2006]. The 16 models were those that were able to submit all the data requested by AeroCom. They were either global chemical transport models, or GCMs (preferably nudged to observed meteorology), with emissions in most cases for the year 2000. The results show that the CSIRO Mk3A model is close to the median of the AeroCom models for sulfate, POM, and dust and is somewhat below the median for BC. Likely reasons for the relatively low BC burden are the assumed emissions of 8.2 Tg per annum, compared to an average of 11.9 Tg per annum for the AeroCom models [*Textor et al.*, 2006], and the assumption of 100% hydrophilic emissions from bio-

Table 4. Comparison of Global-Mean Dry Aerosol Column Burden (in mg m^{-2}) From the Year 2000 of the ALL Ensemble With the Median, Minimum, and Maximum of 16 Models From AeroCom [*Kinne et al.*, 2006]

	CSIRO Mk3A ALL Ensemble	AeroCom Median	AeroCom Minimum	AeroCom Maximum
Sulfate	3.9	3.9	1.8	5.3
POM	3.2	3.3	0.9	5.0
BC	0.28	0.39	0.09	1.0
Dust	42.3	39.1	8.8	57.8
Sea salt	5.6	12.6	4.8	25.8

mass burning. This assumption promotes efficient removal of BC from the atmosphere by in-cloud scavenging. The sea-salt burden in the CSIRO model is much smaller than the median from the AeroCom models and is only slightly larger than the minimum from the AeroCom models. This probably reflects the use of a simple diagnostic sea-salt scheme, which allows no sea salt over land or above the top of the boundary layer over oceans. Even the inclusion of a simple ''background'' sea-salt distribution in these areas would improve the agreement of the sea-salt burden with the median value from the AeroCom models.

[23] Table 5 compares the all-sky midvisible (550 nm) aerosol optical depths (AODs) from the year 2000 of the ALL ensemble with the values from the AeroCom models [*Kinne et al.*, 2006]. Relative to the median AeroCom model, the CSIRO model has a low bias of 38% in total AOD and a smaller low bias of 14% in the fine-mode AOD (which reflects contributions from sulfate, POM, and BC). This supports the suggestion in the previous paragraph that the most serious deficiency in the CSIRO aerosol treatment is the diagnostic treatment of sea salt and its consequent restriction to the marine boundary layer. The relatively low absorption AOD in the CSIRO model is probably due to the relatively low black carbon burden (see Table 4). There may also be a contribution from the fact that we scaled up the SSAs for dust to match the relatively high value of 0.98 at 670 nm used by *Bellouin et al.* [2003] (see footnote d in Table 2). We modified the SSAs because of mounting evidence from observations that the lower SSAs that are typical of older models tend to overestimate the absorption of shortwave radiation by dust [e.g., *Myhre et al.*, 2003; *Yu et al.*, 2004]. After the scaling, the SSA in the midvisible band (497–692 nm) is 1 for small dust and 0.96 for large dust. In future, we plan to use the updated refractive indices from *Myhre et al.* [2003] to recalculate the SSAs for our model.

[24] *Kinne et al.* [2006] gave an estimate of midvisible global-mean AOD of 0.15 from a satellite composite, which considered input from seven different satellite retrievals. They also gave a slightly smaller estimate of 0.135 based on data from the surface-based Aerosol Robotic Network (AERONET) [*Holben et al.*, 2001]. The choice of satellite AOD data for the composite was made by comparison of the satellite retrievals with monthly AERONET statistics in 12 different regions to reduce the effects of cloud contamination or other biases in the retrieval algorithms. The final AOD composite used data from the Moderate Resolution Imaging Spectroradiometer (MODIS) [*Tanré et al.*, 1997; *Kaufman et al.*, 1997], the Advanced Very High Resolution Radiometer (AVHRR) Channel 1 [*Ignatov and Nalli*, 2002] and the Multiangle Imaging Spectroradiometer (MISR) [*Martonchik et al.*, 1998]. Over land, MISR was used, except in the tropical biomass-burning regions, where MODIS was used. Over oceans, MODIS was used in the tropics, and AVHRR was used at middle and high latitudes. Comparison with AERONET data indicates that the satellite composite overestimates AOD by roughly 10% in the global mean, though the overestimate is larger over North America and the tropical oceans (S. Kinne, Aerosol direct radiative forcing with an AERONET touch, submitted to *Atmospheric Environment*, 2007, hereinafter referred to as Kinne, submitted manuscript, 2007). The high bias over tropical oceans is at least partly due to contamination of the MODIS retrieval by thin cirrus [*Yu et al.*, 2006]. Despite some limitations, the satellite composite is attractive because it gives near-global coverage of observations, so in Figure 3 we compare the clear-sky AODs from the model with the composite satellite-retrieved AODs. The clear-sky values from the model are used, since the satellite retrievals generally screen out cloudy pixels. The annual, global-mean clear-sky AOD in the CSIRO model for the year 2000 is 0.093, somewhat lower than the estimates from *Kinne et al.* [2006]. Compared with the satellite composite, the low AOD in the model is apparent over most regions but especially over the tropical oceans, North America, and the Amazon basin. Over the tropical oceans and North America, the high bias in the satellite composite exaggerates the impression of a low bias in the GCM. Besides the sea-salt issue mentioned above, biases in the GCM point to possible problems with the emissions (such as an underestimate of emissions from biomass burning) or other aspects of the aerosol treatment, such as scavenging or radiative properties. The model shows relatively large AODs over oceans to the east of Asia and North America, due to a large contribution from sea salt. This probably reflects the omission of sea-salt scavenging from the model. However, in both the June–August (JJA) and December–February (DJF) seasons, the model qualitatively captures most of the main features of the global AOD distribution, including the major Saharan and Asian dust sources and the industrial sources of the NH.

[25] Aerosol absorption is very sensitive to aerosol mixing state [e.g., *Jacobson* 2001] and absorbing aerosols play a major role in determining surface cooling, atmospheric heating, and consequently the stability and convection in the atmosphere. In our model, POM and BC are assumed to be internally mixed and other species are externally mixed, so it is important to evaluate the modeled SSAs against observations. Point observations from AERONET

Table 5. Comparison of Global-Mean All-Sky Aerosol Optical Depth (Total, Fine-Mode, and Absorption) From the Year 2000 of the ALL Ensemble With the Median, Minimum, and Maximum of the Models From AeroCom [*Kinne et al.*, 2006]

	CSIRO Mk3A ALL Ensemble	AeroCom Median	AeroCom Minimum	AeroCom Maximum
Total	0.079	0.127	0.065	0.151
Fine-mode	0.043	0.050	0.032	0.078
Absorption	0.002	0.005	0.002	0.006

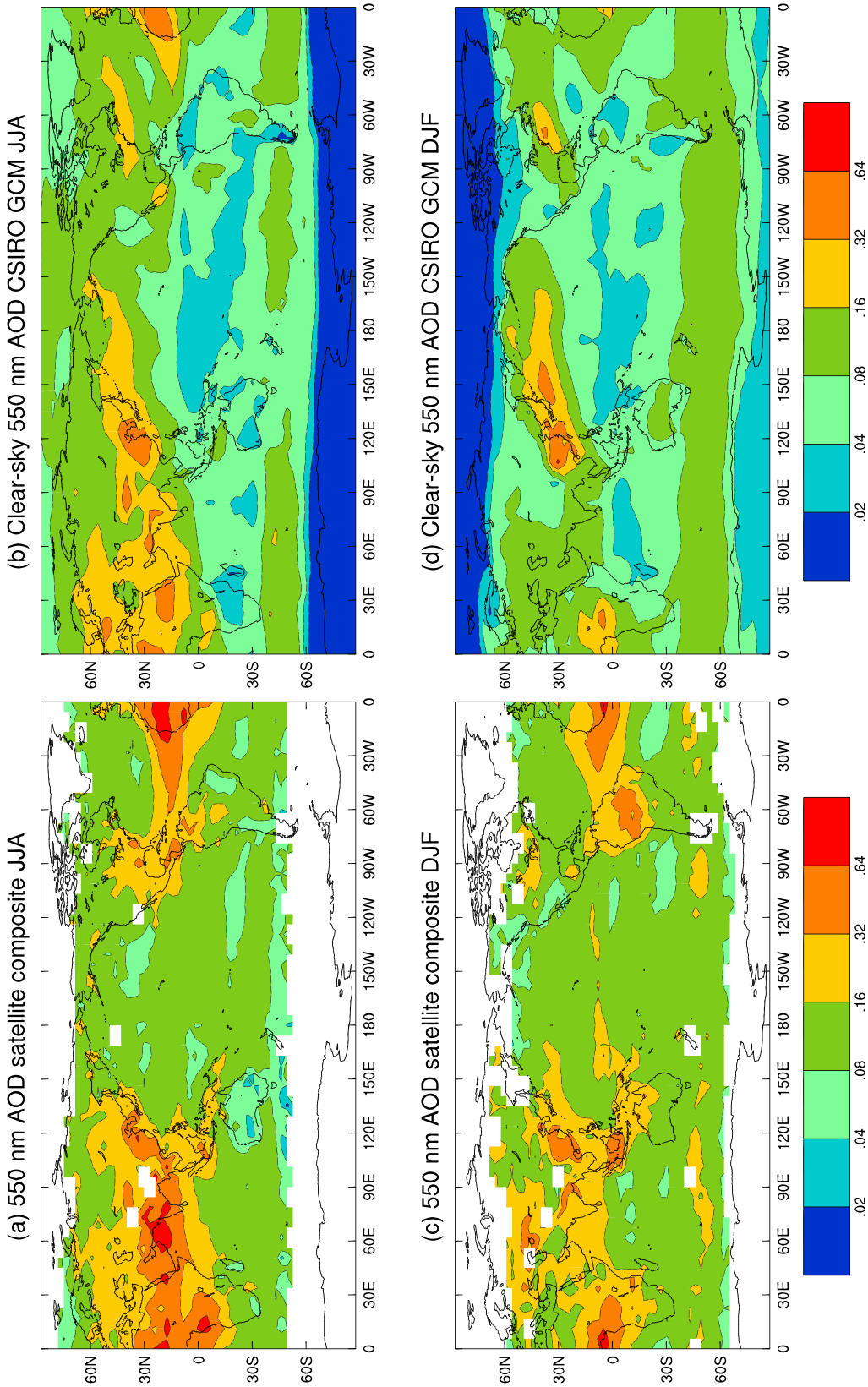

Figure 3. Aerosol optical depth at 550 nm from the satellite composite of *Kinne et al.* [2006] and from year 2000 of the ALL ensemble, for June–August and December–February.

can be used for model evaluation at selected grid points [e.g., *Ghan et al.* 2001]. Recently, a gridded global climatology of aerosol SSA at 550 nm has been constructed by constraining the AeroCom models with measurements from AERONET, to form an AERONET-model composite (Kinne, submitted manuscript, 2007). The new climatology prioritizes statistics from AERONET but falls back on the median reference fields from the AeroCom models [*Kinne et al.*, 2006] if data are unavailable or considered too poor in quality. For example, AERONET SSA data are not used if AOD <0.3, since they are unreliable at low optical depths. In Figure 4, we show the SSAs from the AERONET-model composite and from the CSIRO GCM for the year 2000 for JJA and DJF. The model is broadly successful at capturing the lower SSAs over the tropical biomass-burning regions in both seasons and over South Asia in DJF. Over the remote oceans, the modeled SSA is close to 1, in agreement with the climatology. The most obvious deficiency of the GCM is that it overestimates the SSA over the continental midlatitudes of the NH. This could be explained by underestimated modeled levels of BC in these areas (consistent with the discussion above), or it could indicate a problem with the assumed mixing state of aerosols. Comparison of modeled near-surface BC concentrations with measured values (not shown) suggests that an underestimate of modeled BC concentration is an important factor.

[26] It should be noted that although we have evaluated the radiative properties of the simulated aerosols at the usual reference wavelength of 550 nm, both AOD and SSA are highly wavelength dependent, so more work is required to establish the extent of the errors in the model's broadband aerosol forcing. Indeed, current measurement-based approaches to the assessment of direct aerosol forcing are also subject to considerable uncertainty [*Yu et al.*, 2006], and more observational work is also required to reduce this uncertainty.

2.4.2. Limitations of the Aerosol Treatment

[27] The prognostic aerosol and cloud schemes described above are "bulk" treatments, in the sense that aerosol and cloud species are not resolved in size (except for dust), and there are no interactions among different aerosol species. This is typical of the treatments in the transient GCM runs submitted for the Fourth Assessment Report of the Intergovernmental Panel on Climate Change (IPCC; see http://www-pcmdi.llnl.gov/ipcc/model_documentation/ipcc_model_documentation.php). Prognostic aerosol and cloud treatments in these models are generally fairly simple, due to the heavy computational demands of ensembles of multicentury integrations. More advanced aerosol treatments (incorporating multiple size bins or modes) are seen in some of the aerosol modules that participated in AeroCom [*Textor et al.*, 2006]. A complex treatment incorporating size-resolved hydrometeors and aerosols and detailed cloud-aerosol interactions has also been described [*Jacobson*, 2004], though the task of validating such a scheme on a global scale is very demanding, and the computational requirements would presumably be much larger than for the present model. The cloud and sulfur-cycle treatments in the CSIRO GCM have been evaluated in considerable detail against observations [*Rotstayn*, 1998; *Rotstayn and Lohmann*, 2002b] and were generally found to perform well. Recently, we have greatly improved the global simulation of AOD relative to that shown in Figure 3 by making some fairly minor changes to the model (principally, increasing the carbonaceous aerosol emissions and allowing a background level of sea salt to exist above the top of the marine boundary layer). However, our relatively simple treatments of aerosols and aerosol-cloud interactions have some intrinsic limitations, which we discuss here.

[28] The treatment of sea salt is perhaps the most serious limitation of the aerosol module because it is not prognostic. Thus while sea-salt concentrations in the marine boundary layer can respond to changes in local wind speed, they cannot respond to changes in precipitation or transport. It is our intention to upgrade the model to include a prognostic treatment, although it should be noted that there are large variations among the different source functions that have been used [*Lewis and Schwartz*, 2004; *Textor et al.*, 2006]. Since sea salt concentrations are large in the SH and are expected to change with climate, it is possible that the simple treatment used here may have influenced our results. Our simulations do show increasing trends of sea salt concentration over the Southern Ocean (south of about 50°S) due to increasing wind speed there. It is possible that this has affected climatic trends over southern Australia, perhaps via effects on the Southern Annular Mode, but it seems less likely to have influenced the tropics and subtropics (which are the main focus of this study).

[29] Although our mineral dust treatment is prognostic, our model does not currently include longwave radiative effects of dust, which are thought to be substantial [e.g., *Zhang and Christopher* 2003]. We have not conducted tests to determine whether our results are sensitive to the inclusion of dust in the model, but it is possible that omission of dust longwave forcing may have affected our results. Also, the modeled dust emissions are a function of wind speed and soil moisture [*Ginoux et al.*, 2004], but changes in dust emission due to land-use changes are not included in our simulations. Perhaps for this reason, the dust burden over Australia does not vary appreciably over the period of our analysis (averaging 84.9 mg m^{-2} during the 1950s and 84.2 mg m^{-2} during the 1990s). For this reason, we do not believe that dust feedbacks have had a large impact on Australian climatic trends in our simulation, but to show this rigorously we would have to perform another ensemble of runs with dust emission turned off.

[30] Several other aspects of our "bulk" aerosol treatment are very simplified, although they are typical of current GCMs. For example, different aerosol modes cannot interact (e.g., by coagulation or heterogeneous chemistry), and BC and POM are converted from hydrophobic to hydrophilic states with a fixed e-folding time, regardless of conditions. The treatment of secondary organic aerosol is also crude, since conversion to POM is assumed to occur instantaneously, which would alter the spatial distribution of POM, and gas photochemistry is not treated in the model. Emissions of POM and BC are assumed to be hydrophilic or hydrophobic with specified fractions, whereas in reality the hydrophilic fraction depends on particle size. Nitrate aerosol is currently omitted, although there is evidence that it is has significant direct and indirect effects on climate [e.g., *Adams et al.*, 2001; *Ishizaka and Adhikari*, 2003]. Cloud droplet number concentration in the stratiform-cloud scheme is determined as an empirical function of aerosol

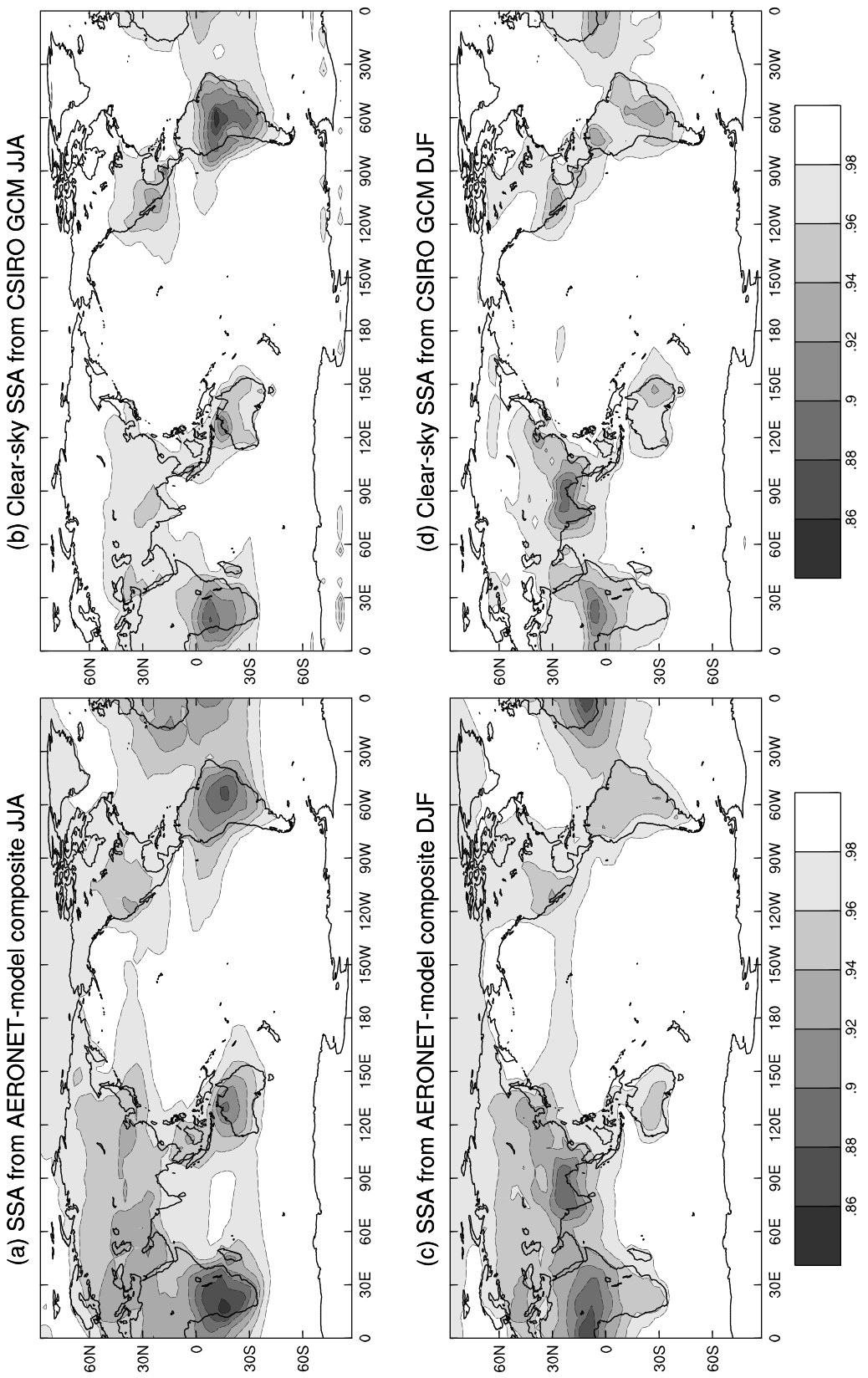

Figure 4. Aerosol single scattering albedo at 550 nm from the AERONET-model composite, and from year 2000 of the ALL ensemble, for June–August and December–February.

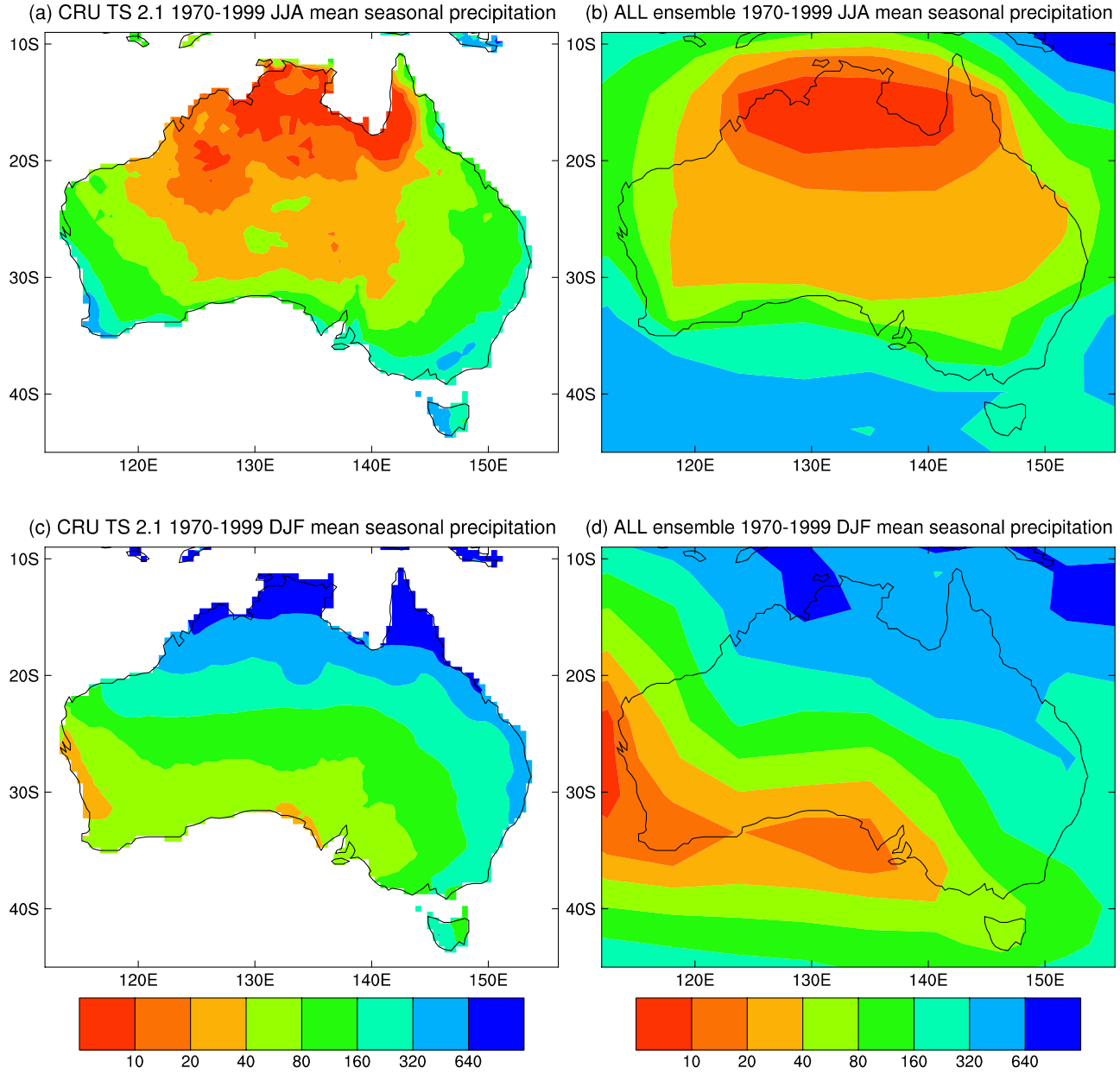

Figure 5. Observed and modeled Australian seasonal precipitation (in mm) for JJA and DJF, averaged over the period 1970–1999.

mass, which neglects much of the subtle physics and chemistry involved in cloud droplet nucleation [e.g., *Lance et al.* 2004]. There is considerable variation among existing parameterizations of cloud droplet number concentration, and our results are likely to be quite sensitive to the particular scheme we have used in these simulations. Interactions between aerosols and convective rainfall are neglected, even though observations [*Rosenfeld and Lensky*, 1998], detailed cloud modeling [*Khain and Pokrovsky*, 2004], and sensitivity tests with GCMs [*Menon and Rotstayn*, 2006] all suggest they are likely to be important. In general, the problem of treating unresolved subgrid-scale cloud processes in GCMs leads to many uncertainties [*Pincus and Klein*, 2000; *Rotstayn*, 2000; *Randall et al.*, 2003], and this has motivated some authors to develop models that allow multiple subgrid clouds to exist in each GCM grid box [*Khairoutdinov and Randall*, 2001; *Jacobson*, 2004]. These approaches are much more computationally demanding but hold promise for future climate-change simulations.

[31] Some aerosol-related climate feedbacks are also omitted from our simulations. These include temperature-dependent changes in oceanic DMS concentrations [e.g., *Charlson et al.*, 1987; *Gabric et al.*, 2003], since we prescribe this field based on measurements taken in the modern-day climate. Natural emissions of terpenes are also expected to change with climate [*Kanakidou et al.*, 2005], but in the model these are prescribed.

2.5. Simulation of Australian Rainfall and Cloudiness

[32] The global distribution of annual rainfall from an earlier version of the Mk3A CSIRO GCM was shown by

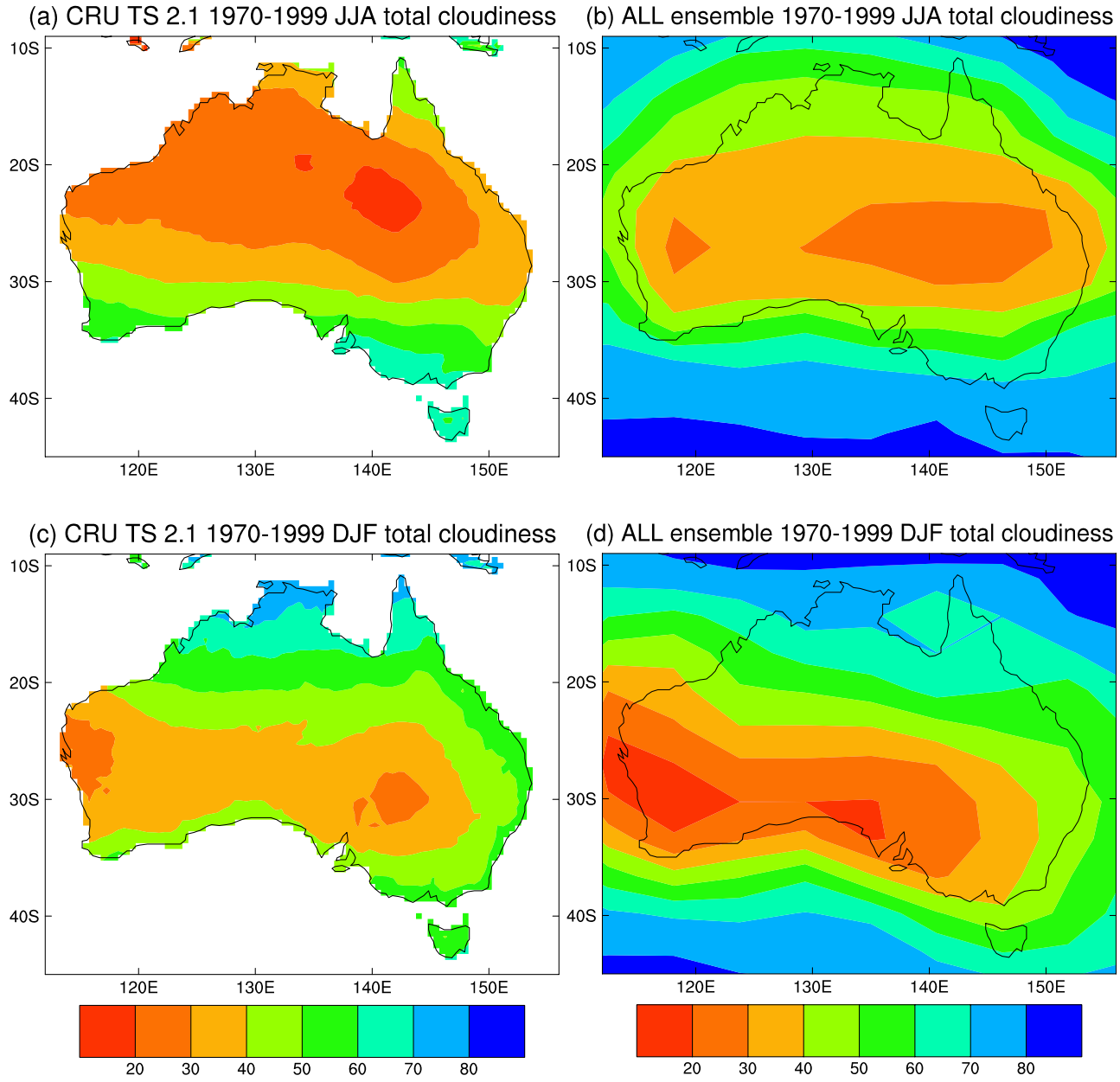

Figure 6. Satellite-retrieved and modeled Australian cloudiness (in %) for JJA and DJF, averaged over the period 1984–2000.

Rotstayn and Lohmann [2002a], and it was found that the model was broadly successful at simulating the main features of the observed global climatological rainfall pattern. This is also true of the current version (not shown), but since the present study focuses primarily on Australian rainfall trends, it is important to check whether the model can simulate the regional rainfall patterns over Australia. Figure 5 shows observed and modeled seasonal precipitation for JJA and DJF, averaged over the period 1970–1999. The observations are high-resolution (0.5°) gridded data from the Climatic Research Unit (CRU), known as CRU TS 2.1 [*Mitchell and Jones*, 2005], and the modeled values are the ALL ensemble mean. In both seasons the model is broadly successful at capturing the spatial pattern of precipitation, although it tends to be too dry over southern Australia, especially over the southwestern corner in DJF. Also, the monsoonal rainfall over the northeastern corner is underestimated in DJF. Overall, this is an encouraging result for a low-resolution GCM.

[33] The distribution of global cloudiness in an earlier version of the CSIRO GCM was compared with observations by *Rotstayn* [1998] and was found to be generally satisfactory. Here, we continue our focus on the Australian region and compare observed and modeled cloudiness for JJA and DJF, averaged over the period 1970–1999 (Figure 6). The observed values are from CRU TS 2.1 and are based on surface observations. In both seasons the model captures the broad pattern of cloudiness over Australia, but there are problems in the detail. In JJA the model somewhat underestimates cloudiness over southwestern Australia and overestimates it over northern Australia. In DJF the modeled cloudiness is fairly realistic

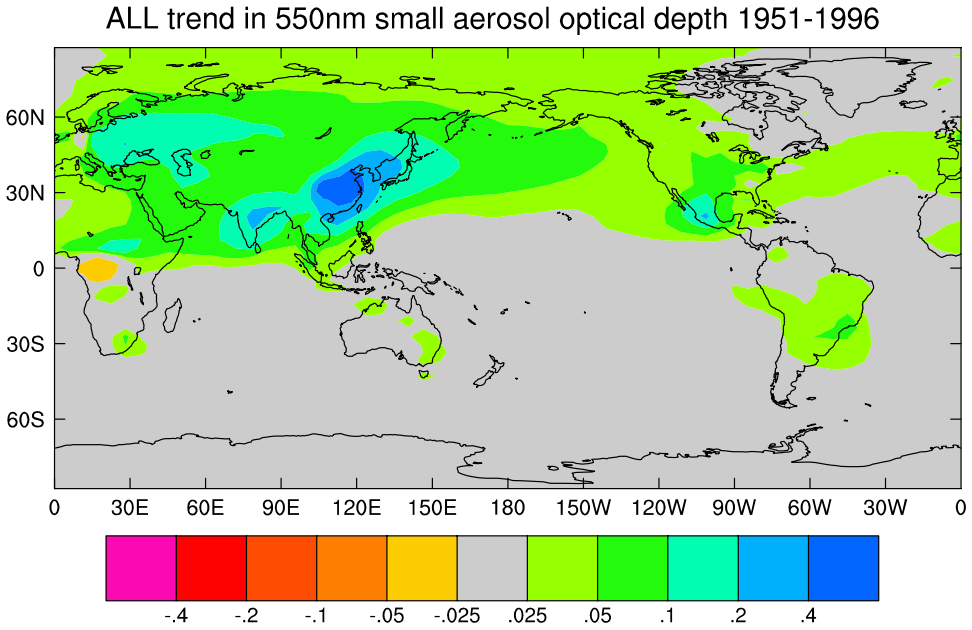

Figure 7. The 1951–1996 trends in small-particle aerosol optical depth at 550 nm (AOD units per century) from the ALL ensemble.

over northern Australia but too low over southern Australia. The low bias over southern Australia in DJF is similar to the result for rainfall, suggesting a common underlying dynamical bias. We have found that the SH midlatitude storm tracks in the model tend to lie too far to the south; the effects of this bias are noticeable in the next section, where observed and modeled trends are compared.

3. Observed and Modeled Trends in the Australian Hydrological Cycle 1951–1996

[34] Here and in the following sections, we focus on the period 1951–1996. We take 1951 as the starting point of the analysis, since global aerosol levels began to increase steeply after 1950. We take 1996 as the end point of the analysis, since in our model the average optical depth of anthropogenic aerosol over the region we defined as Asia (in section 2.3) reached a maximum in 1996. We expect that the impact of anthropogenic aerosols on the Australian hydrological cycle in our model is predominantly due to the large Asian aerosol haze, rather than the much smaller amounts of aerosol that exist over Australia itself. For example, Figure 7 shows the trend in small-particle aerosol optical depth during 1951–1996 from the ALL ensemble. Small particles are assumed to be sulfate, POM, and BC, so this quantity is a good proxy for anthropogenic aerosol optical depth [e.g., *Kaufman et al.* 2005]. Figure 7 shows the predominance of anthropogenic aerosol trends in the NH relative to those in the SH and in particular of those over Asia relative to those over Australia. The predominant impact of Asian aerosols in our model is confirmed by a sensitivity test, in which only Asian anthropogenic aerosols are allowed to vary with time (see section 6).

3.1. Spatially Averaged Trends

[35] Table 6 shows observed and modeled trends in rainfall, cloudiness, and DTR, averaged over Australia. The observations are from CRU TS 2.1 [*Mitchell and Jones*, 2005] and from the high-quality rainfall [*Lavery et al.*, 1997] and temperature [*Della-Marta et al.*, 2004] networks of the Australian Bureau of Meteorology. Statistical significance was assessed by a two-sided t-test using the 46 continent-averaged annual means as independent data points. The observed rainfall trends are not significant, due to contrasting areas of increasing and decreasing rainfall that are discussed below. There is a much stronger decrease of DTR in the CRU observations than in the Bureau's observations. In part, this probably reflects the fact that the Bureau's observations exclude sites that were thought to be affected by increasing urbanization, whereas the CRU observations do not. Using the annual Australian DTR values from the Bureau, we find a correlation with the annual Australian cloudiness observations of −0.89, close to the value of −0.90 previously reported [*Dai et al.*, 1997]. Using the DTR values from the CRU, we obtain an even stronger correlation of −0.95, but this is probably because DTR observations were used to derive estimates of cloudiness in regions of missing cloud observations in the CRU data [*Mitchell and Jones*, 2005]. While the details of the cloudiness trends are open to question, the veracity of an

Table 6. Observed and Ensemble-Mean Modeled Trends in Annual Rainfall, Cloudiness, and Diurnal Temperature Range (DTR), Averaged Over Australia for the Period 1951 to 1996[a]

	Annual Rainfall, mm/century	Cloudiness, %/century	DTR, K/century
Observed (CRU)	38	*10.9*	*−2.43*
Observed (BoM)	68		**−0.78**
ALL ensemble mean	**92**	**3.1**	*−1.03*
AXA ensemble mean	−35	*−4.6*	0.21

[a]Trends significant at 10% (1%) are shown in bold (italic) font. Observations are from the CRU TS 2.1 data set and the Australian Bureau of Meteorology (BoM).

overall increasing trend is supported by the increasing rainfall trend and by the strong correlation with the Bureau's DTR measurements. For all three quantities (rainfall, cloudiness, and DTR), Table 6 shows that the ALL ensemble agrees better with the observations than the AXA ensemble does.

[36] The trend of increasing cloudiness and rainfall in the ALL ensemble may also be consistent with the observed trend of decreasing Australian pan evaporation reported recently [*Roderick and Farquhar*, 2004]. The shortwave radiative impact of increased cloudiness and column water vapor and the effect of a moister lower atmosphere would contribute to decreased pan evaporation [*Roderick and Farquhar*, 2002]. However, a detailed analysis would also need to consider the offsetting longwave effects of increased cloudiness, as well as any changes in wind speed and direct aerosol effects over Australia.

3.2. Rainfall and Cloudiness Trends in Detail

[37] In this subsection, we consider the spatial patterns of the modeled Australian rainfall and cloudiness trends and compare them with observed trends from CRU TS 2.1. We assess statistical significance based on a two-sided t-test using the 46 annual means from each grid box as independent data points. There is an argument that in the tropical and subtropical parts of Australia, it makes sense to time-average the rainfall data so that each wet season (November to April) constitutes an independent data point. (For example, each year might run from November to October, rather than using calendar years.) However, when we tested this approach, it made little difference to the results.

[38] Figure 8 shows trends in annual rainfall over Australia from observations, from the ALL and AXA ensemble means, and the differences between the ALL and AXA ensemble means. The observed rainfall (Figure 8a) shows increases in the northwestern and central parts of Australia and decreases in the east, southeast, and southwest. On the basis of a two-sided t-test using the 46 annual means from each grid box as independent data points, we find that the observed trends during 1951–1996 are statistically significant only over limited areas, mostly in the northwest. The observed decrease of rainfall in the southwest has been linked to changes in the Southern Annular Mode (discussed in section 1), and this suggests possible links to increasing greenhouse gases or Antarctic ozone depletion, but there are still ambiguities in making this connection [*Timbal et al.*, 2006]. Other recent studies have suggested land-cover change [*Pitman et al.*, 2004] or natural multidecadal fluctuations [*Cai et al.*, 2005c] as possible causes of the rainfall decrease in the southwest. The observed rainfall decrease along the east coast may reflect an increased frequency of El-Niño events in the late 20th century, which could be related to increased greenhouse gases (at least in part), but detailed studies are lacking. The observed trends show little statistical significance there and may simply be due to natural fluctuations, especially in view of the fact that the 1950s were unusually wet over eastern Australia.

[39] Few studies have attempted to explain the increasing rainfall trend over northwestern and central Australia. A rainfall response with some similarity to the observed increase was obtained in a recent modeling study in which Australian surface albedos were decreased [*Wardle and Smith*, 2004], though the prescribed decreases were much larger than could be justified based on current knowledge, so the authors left the cause of the rainfall increase as an open question. *Whetton et al.* [1996] compared rainfall changes in five enhanced greenhouse climate simulations that used coupled OAGCMs and five that used atmospheric GCMs with mixed-layer ocean models. The coupled experiments mostly gave a decrease of summertime rainfall over northwestern and central Australia, whereas the mixed-layer experiments mostly gave an increase (in better agreement with the observed 20th century trends). The authors noted that the stronger overall warming of the NH in the coupled models is expected to lead to a similar hemispheric imbalance in rainfall [*Murphy and Mitchell*, 1995]. The hemispheric imbalance is due to the much smaller proportion of land in the SH, causing a delayed warming there relative to the NH. In their coupled GCM simulation, *Murphy and Mitchell* [1995] found a shift in the mean Hadley circulation, with increased ascent to the north of the equator and increased subsidence to the south. This shift is of the opposite sense to that found in climate-change experiments forced by aerosol effects alone [e.g., *Williams et al.* 2001]. *Whetton et al.* [1996] pointed out that the warming of the SH was underestimated by the early coupled models that they considered, so they cautioned against giving too much weight to these models, despite their in-principle advantages over mixed-layer models. However, they were unsure why the largest differences between the simulated rainfall changes of the coupled and mixed-layer experiments should occur in the tropics and subtropics of the Australian region.

[40] The ALL ensemble mean shows increasing rainfall over most of the continent, with the strongest rainfall increase in the northwest corner (Figure 8b). The AXA ensemble shows mostly decreasing rainfall, especially in the northwest (Figure 8c). Overall, the ALL ensemble agrees better with the observations, even though it does not capture the decreasing rainfall along the east coast. The ALL ensemble shows decreasing rainfall to the south of Australia, instead of over southern Australia as seen in the observations. This reflects the fact that the SH storm tracks in the Mk3A model are too far south, so the expected "signature" of their poleward shift [*Yin*, 2005] also appears too far south. The differences between the ALL and AXA ensembles (i.e., the effect of anthropogenic aerosols) show statistical significance over much of the continent (Figure 8d). The inability of the AXA simulation to capture the increase in rainfall centered over northwestern Australia is consistent with the results from *Whetton et al.* [1996] and also with another study in which seven out of eight coupled OAGCMs forced only by greenhouse gases showed a decrease of wet season rainfall over northwestern Australia [*Whetton et al.*, 2001].

[41] The observed rainfall increase over northwestern and central Australia is primarily a summertime phenomenon, since it is mostly in that season that the monsoonal rains occur (both in the real world and in the model). Figure 9 shows the observed and modeled rainfall trends for the DJF season. The pattern in the AXA ensemble (Figure 9c) shows decreases in the northwest and increases in the north and east and is negatively correlated with the observed pattern (Figure 9a). Although the ALL ensemble (Figure 9b) does not capture the rainfall decrease over eastern Australia, the

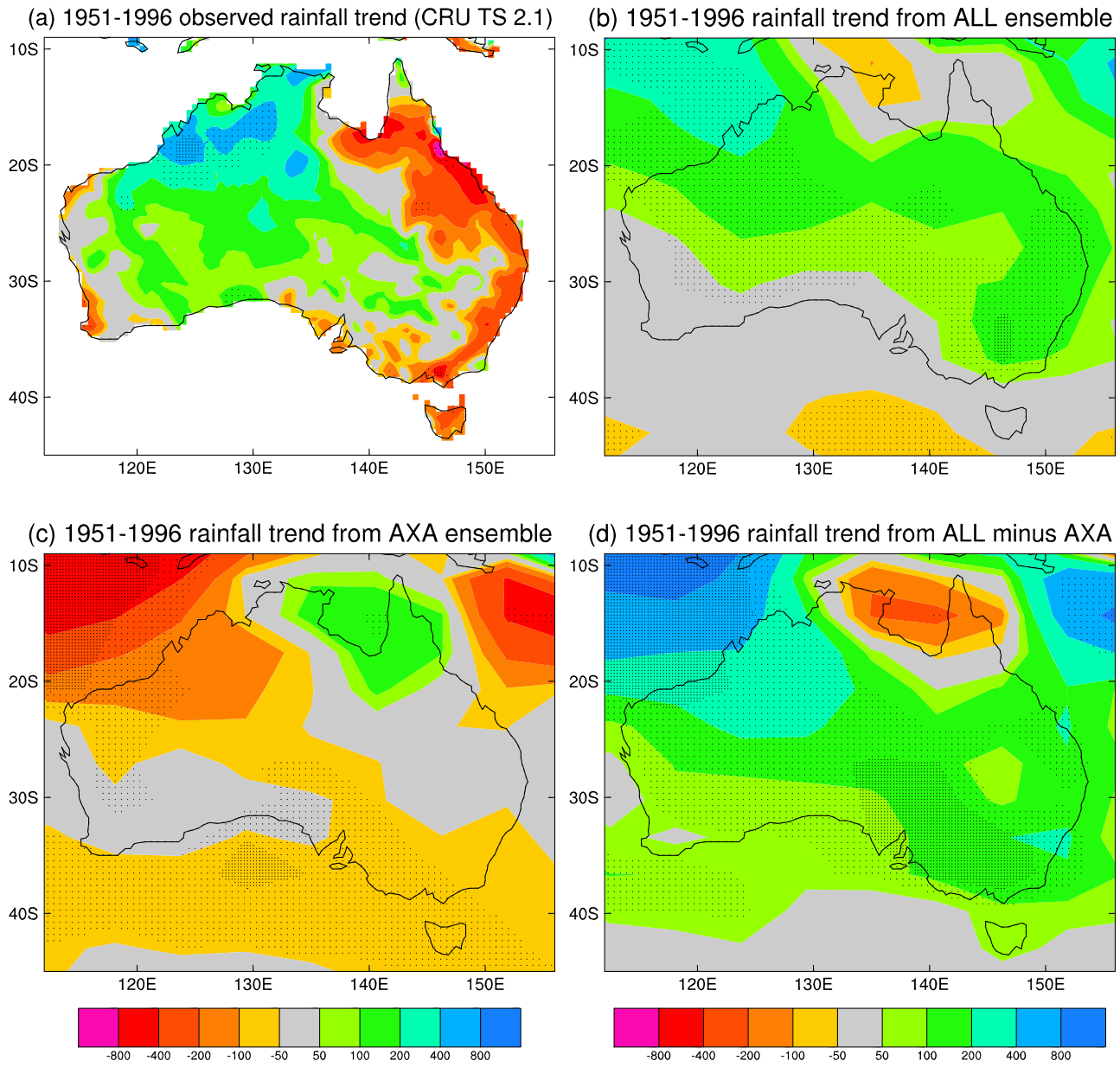

Figure 8. Observed and modeled annual rainfall trends (mm per century) over the Australian region for the period 1951 to 1996. Modeled trends are ensemble means (ALL and AXA) and the difference between them (ALL minus AXA). Light (heavy) stippling shows areas where the trends are significant at 10% (1%).

difference between the ALL and AXA ensembles (Figure 9d) shows that including aerosols in the model has reduced the increase of summertime rainfall in the northeast, substantially improving the agreement with the pattern of observed trends.

[42] Figure 10 shows cloudiness trends from observations, from the ALL and AXA ensemble means, and the difference between the ALL and AXA ensemble means. The observed cloudiness trends show increases over most of the continent, except for parts of the southwest and southeast, and are statistically significant over wide areas. As discussed above, the observations are very uncertain, but the veracity of an overall increasing trend is supported by the decreasing DTR trend. Over northwestern and central Australia, the observed cloudiness trends are of the same sign as the observed rainfall trends, but there are some regions (notably in the northeast) where the cloudiness trends are of opposite sign to the rainfall trends. The ALL ensemble mean shows increasing cloudiness over most of the continent, whereas the AXA ensemble shows decreasing cloudiness over the entire continent (covering a much larger area than the rainfall decrease in the AXA ensemble). The differences between the ALL and AXA ensembles (Figure 10d) show that inclusion of anthropogenic aerosols in the model causes an increasing cloudiness trend over almost the entire continent. Overall, the ALL ensemble agrees much better with the observed trends, except that it does not capture the observed decreasing trends in the

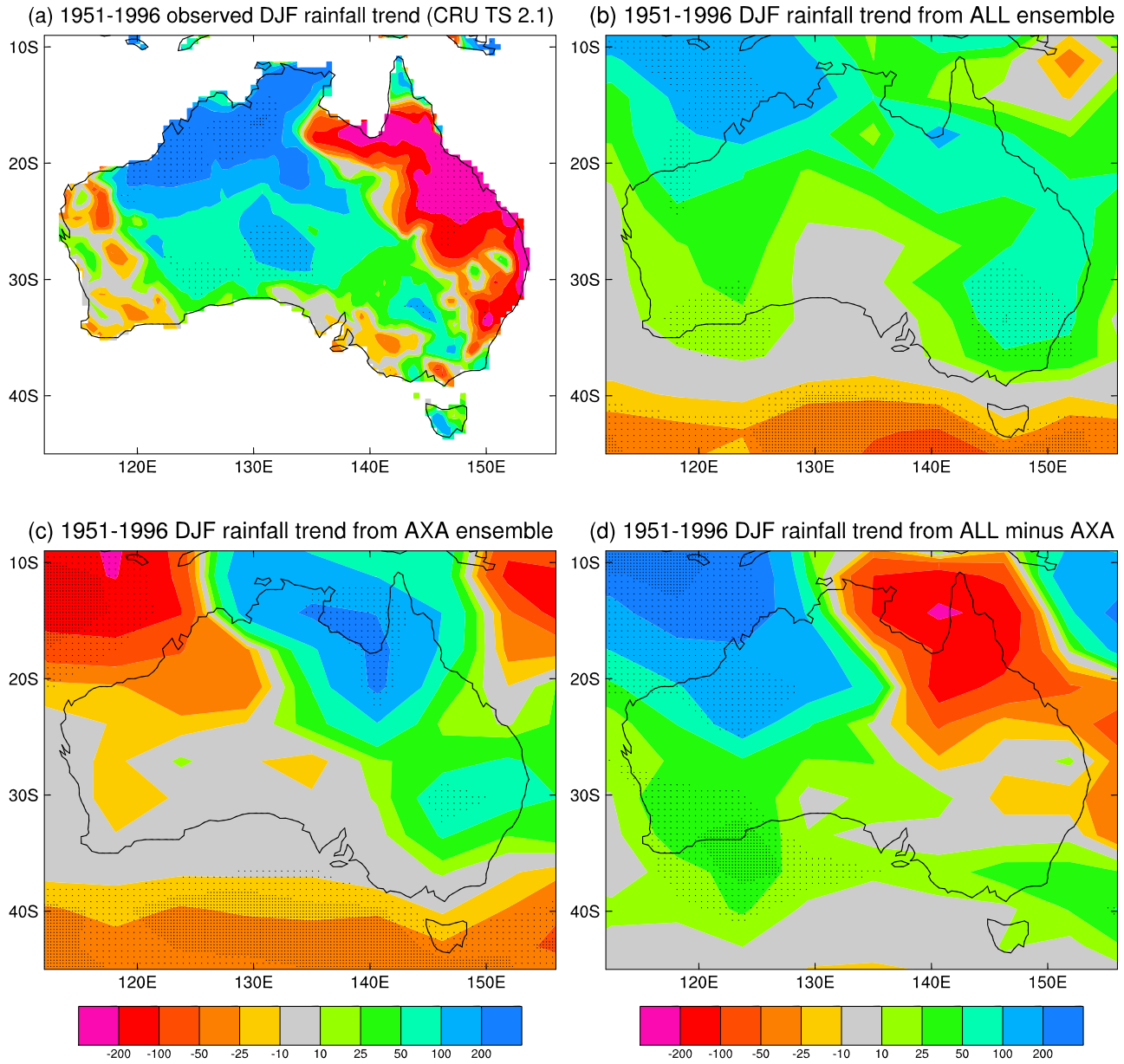

Figure 9. Observed and modeled DJF seasonal rainfall trends (mm per century) over the Australian region for the period 1951 to 1996. Modeled trends are ensemble means (ALL and AXA) and the difference between them (ALL minus AXA). Light (heavy) stippling shows areas where the trends are significant at 10% (1%).

southwest and southeast (which are broadly consistent with decreasing observed rainfall in those regions). Again, this probably reflects the SH storm tracks being too far south in the model, which results in the decreasing midlatitude cloudiness trend falling to the south of the continent (Figure 10b).

4. Dynamical Aspects of the Trends

4.1. Surface Temperature and Atmosphere

[43] The different responses of the Australian hydrological cycle between the two ensembles are caused by different patterns of regional temperature change and the resulting changes in atmospheric circulation. Figure 11 shows that whereas the surface in the AXA ensemble warms everywhere in the region surrounding Australia, the inclusion of aerosols in the ALL ensemble causes regional cooling trends over parts of Asia and the Pacific Ocean, which are qualitatively similar to the regions of cooling in the surface observations. Over China, the model (Figure 11c) agrees better with the high-resolution observations (Figure 11b) than with the HadCRUT2 observations (Figure 11a), which show only a small area of cooling there. Over South Asia, the modeled region of cooling is displaced southwards relative to the observed cooling, perhaps because of the low horizontal resolution of the model and its highly smoothed representation of surface topography. Regions of observed surface cooling in the Pacific Ocean (Figure 11a) are qualitatively captured by the

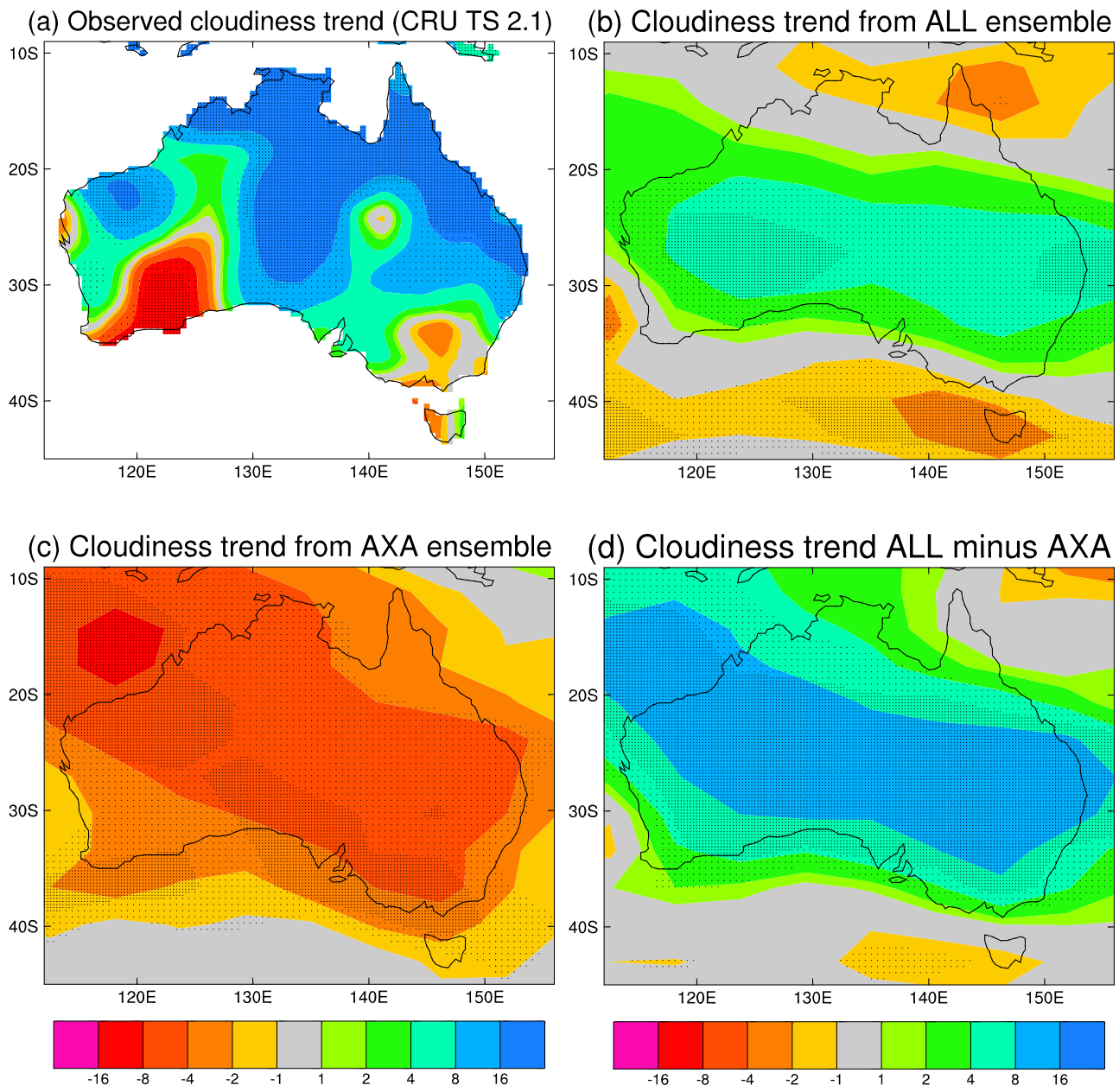

Figure 10. Observed and modeled cloudiness trends (% per century) over the Australian region for the period 1951 to 1996. Modeled trends are ensemble means (ALL and AXA) and the difference between them (ALL minus AXA). Light (heavy) stippling shows areas where the trends are significant at 10% (1%).

ALL ensemble (Figure 11c), although the modeled cooling in the North Pacific is split into two separate regions. In the ALL ensemble, the warming trend of SST in the southeastern tropical Indian Ocean is greater than that in the northwestern tropical Indian Ocean (Figure 11c), promoting stronger convection and rainfall over Australia. The SST pattern in Figure 11c resembles the "negative" phase of the Indian Ocean Dipole, which has previously been linked to increased rainfall over Australia on interannual timescales [*Ashok et al.*, 2003; *Cai et al.*, 2005a]. In the AXA ensemble the SST pattern is reversed, with a greater warming trend of SST in the northwestern tropical Indian Ocean than in the southeastern tropical Indian Ocean (Figure 11d). Note that changes in ocean dynamics make an important contribution to the different SST trends in the two ensembles (see section 4.2). As expected for an eight-member ensemble, there is less spatial variability in the ALL ensemble than in the observations.

[44] Trends in atmospheric circulation from the two ensembles are shown in Figure 12. For the ALL ensemble, the trend in vertical motion at 500 hPa (Figure 12a) and the associated divergent winds at 220 hPa show that convection over the Indian Ocean has moved away from the northwestern tropical Indian Ocean and towards the southeast, closer to Australia (220 hPa is roughly the level of convective outflow, so the trend of divergent wind vectors at this

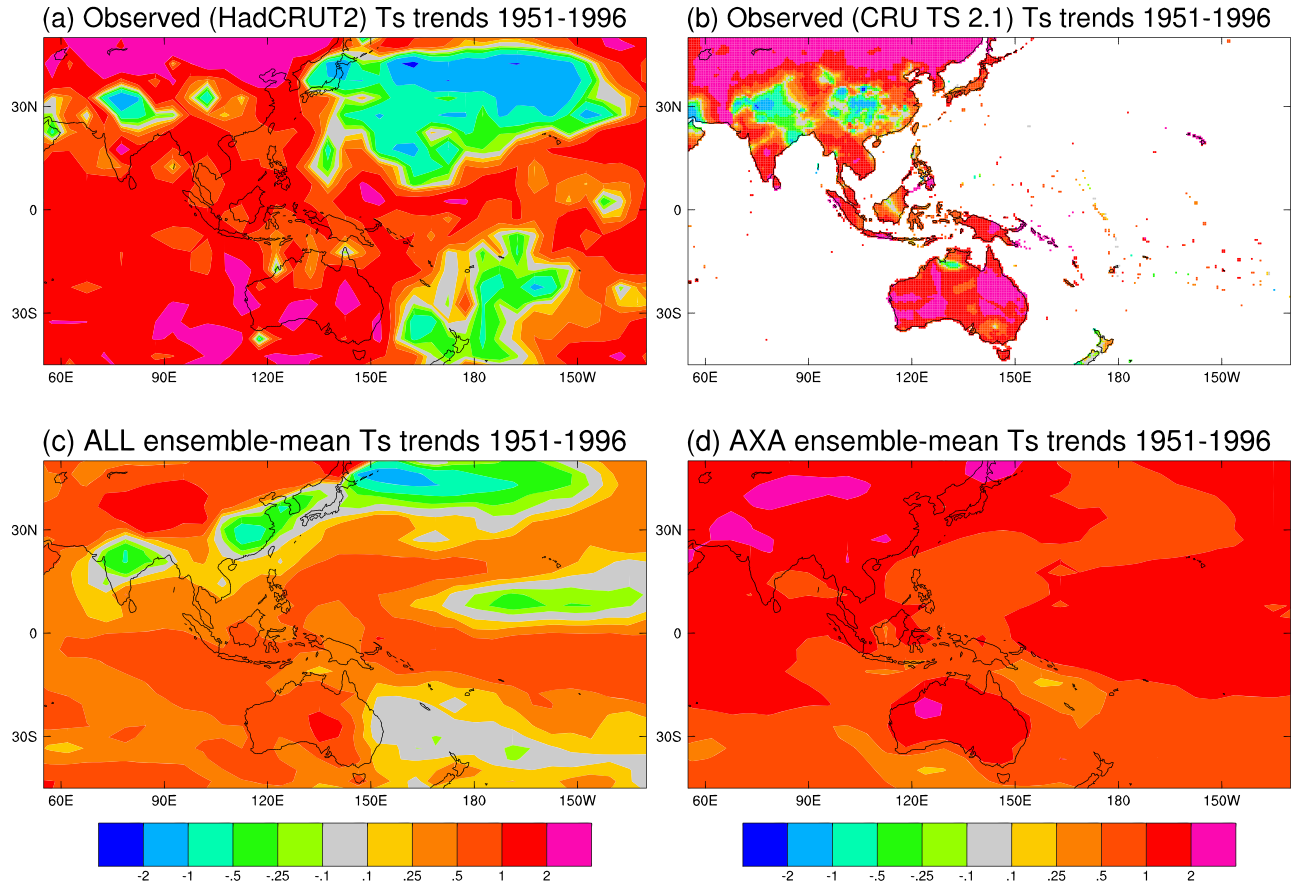

Figure 11. T_s trends in K/century for the period 1951 to 1996. Observations are from (a) the global 5° HadCRUT2 data set [*Jones and Moberg*, 2003; *Rayner et al.*, 2003] and (b) the high-resolution (0.5°) CRU TS 2.1 data set over land [*Mitchell and Jones*, 2005]. Modeled trends are means from the (c) ALL and (d) AXA ensembles. T_s represents sea surface temperature over oceans and surface-air temperature over land.

level shows the reverse of the trend in convective activity). Figure 12c shows the trends in near-surface winds for the ALL ensemble, which are consistent with the vertical motion trends (Figure 12a), in that they flow toward the centers of increased convection. In particular, there is convergence of the near-surface winds into a region south of Sumatra, resulting in a center of strongly increasing ascent there. This feature also affects Australia, especially the northwestern parts, where the observed trend of increasing rainfall is strongest (Figure 8a). Over the Pacific Ocean, the ALL ensemble shows a southward shift of convection across the Equator, consistent with the T_s trends (Figure 11c), and reminiscent of earlier results in GCM simulations forced by aerosol effects [e.g., *Rotstayn et al.* 2000b].

[45] Dynamically, the meridional temperature gradient over the Indian Ocean and southern Asia affects the meridional pressure gradient, which is the driving force of the low-level monsoonal winds [*Webster and Fasullo*, 2003]. Zonally averaged trends in T_s and sea level pressure (SLP) over a region covering the tropical Indian Ocean and southern Asia are shown in Figure 13. The trend in the meridional T_s gradient in the ALL ensemble (Figure 13a) shows the influence of Asian aerosol-induced cooling and agrees well with that in the observations, even though this ensemble generally underestimates the warming over this region. The trend in the meridional SLP gradient in the ALL ensemble (Figure 13b) is dynamically consistent with the T_s trend and enhances the monsoonal flow toward Australia. The AXA ensemble shows a trend in meridional SLP gradient of the opposite sense to that in the ALL ensemble. This is consistent with increased Asian continental heating in the AXA ensemble, which is mainly forced by increasing greenhouse gases.

[46] We have not shown observed trends in the meridional SLP gradient in Figure 13b because we found very large differences among the available data sets in this region (not shown). We considered the NCEP/NCAR reanalysis [*Kalnay et al.*, 1996], the ERA-40 reanalysis from 1958 [*Uppala et al.*, 2005], a new global historical SLP data set (HadSLP2) [*Allan and Ansell* 2006], and another historical SLP data set [*Smith and Reynolds*, 2004], which covers oceanic areas only. Large differences in the data make it difficult to draw firm conclusions regarding the realism of our modeled SLP trends. *Gillett et al.* [2005] also showed large differences in SLP trends among different data sets.

[47] Consistent with the above, the trends in vertical motion and near-surface winds are also very different in the AXA ensemble. The winds over the Indian Ocean (Figure 12d) show a tendency to flow toward Asia, forced by the trend in meridional SLP-gradient (Figure 13b). There

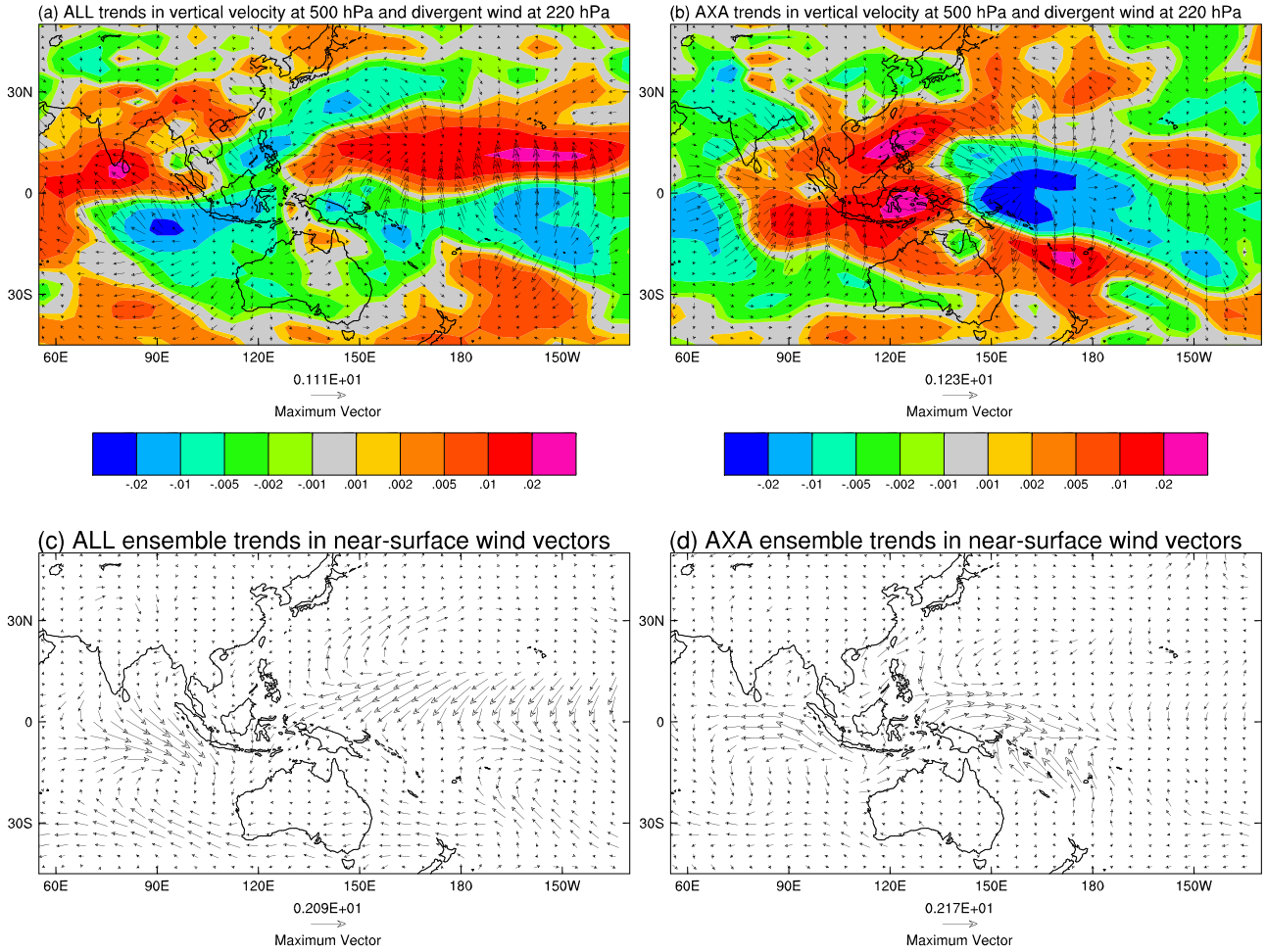

Figure 12. Trends in atmospheric circulation for the period 1951 to 1996: Vertical velocity at 500 hPa (shaded) in Pa/s/century and divergent component of horizontal wind (vectors) at 220 hPa in m/s/century from the (a) ALL and (b) AXA ensembles. Cool (warm) colors denote increasing ascent (subsidence). Trends in near-surface winds in m/s/century from the (c) ALL and (d) AXA ensembles.

is a trend of increased subsidence over most of tropical Australia (Figure 12b), consistent with the reversed trends in the meridional T_s and SLP gradients (Figure 13). The increased subsidence over Australia is also consistent with an El Niño-like SST trend pattern in the Pacific Ocean, as seen in some climate-change simulations forced by increasing levels of greenhouse gases [*Meehl and Washington*, 1996; *Cai and Whetton*, 2000].

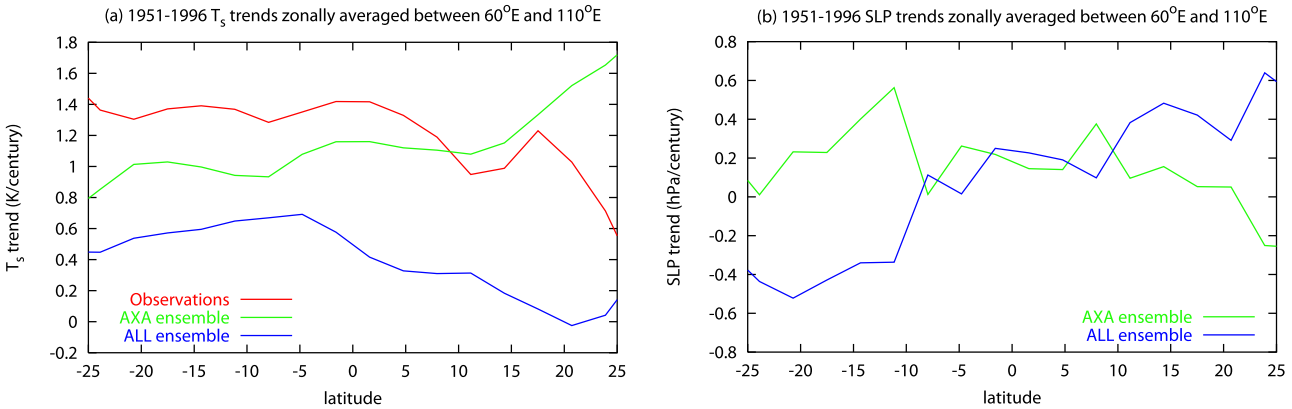

Figure 13. The 1951–1996 trends in (a) T_s and (b) SLP, zonally averaged between 60°E and 110°E, from the ALL and AXA ensembles. Also shown in Figure 13a are the zonally averaged HadCRUT2 observed T_s trends. The region covers most of the tropical Indian Ocean and southern Asia.

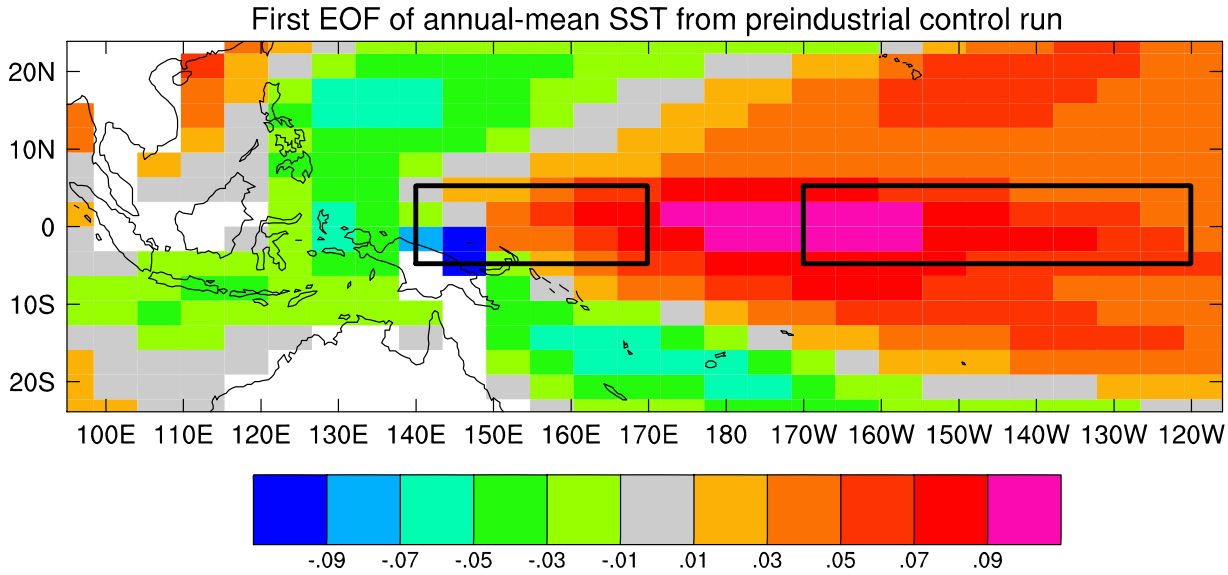

Figure 14. First empirical orthogonal function of annual-mean SST over the tropical Indo-Pacific region, from the preindustrial control run that was used to initialize the transient runs. The two boxes are the Niño 3.4 and tropical western Pacific boxes that are routinely used to define El Niño or La Niña-like states. For the GCM, we use two boxes that are shifted approximately 20° to the west to better agree with the model's ENSO-like mode; see text for details.

[48] A simple way to quantify the extent to which the Pacific SST trend pattern is El Niño-like is to compare the SST trends for the Niño 3.4 region (170°W–120°W, 5°S–5N°) and for a box in the tropical western Pacific (140°E–170°E, 5°S–5N°) [e.g., *Philander* 1990]. However, in common with many coupled OAGCMs [*Knutson et al.*, 1997; *Meehl et al.*, 2001; *Cai et al.*, 2003b], our model suffers from an eastern Pacific cold tongue that extends too far to the west, with the result that the simulated El Niño is also displaced to the west. Figure 14 shows the first empirical orthogonal function (EOF) of annual mean SST from the (unforced) preindustrial control run that we used to initialize the transient runs. It indicates that the model's major mode of variability in the Pacific Ocean resembles El Niño (including the familiar "horseshoe" pattern), but the SST maximum is displaced roughly 20° to the west of the Niño 3.4 region. Thus it is more appropriate to compare the modeled SST trends in two boxes shifted roughly 20° westward of those described above. To coincide with the model's grid box boundaries, we defined the eastern (shifted Niño 3.4 box) as approximately 172°E–138°W, 6°S–6°N and the western box as approximately 121°E–149°E, 6°S–6°N. In the AXA ensemble, the difference between the SST trends (eastern box minus western box) is +0.68 K/century, confirming a strong El Niño-like warming trend. In the ALL ensemble, the difference is −0.02 K/century, showing that the inclusion of anthropogenic aerosol forcing has caused the warming pattern to be weakly La Niña-like. This is consistent with the argument that the El Niño-like warming pattern in simulations forced by increasing greenhouse gases is caused by subduction of warm surface waters that originate in the extratropical North Pacific several decades earlier [*Cai and Whetton*, 2000]. A weaker surface warming in the extratropical North Pacific when anthropogenic aerosols are included thus leads to a more La Niña-like pattern of SST change in the tropical Pacific. (This is discussed further in section 6.) The more La Niña-like SST trend pattern in the ALL ensemble is also broadly consistent with the simulated trend of increasing rainfall over most of eastern Australia when anthropogenic aerosol forcing is included (Figure 8d).

[49] Over the tropical Indian Ocean, the dynamical changes induced by aerosols in our model are similar in both DJF and JJA. Figure 15 shows the differences (ALL minus AXA) in the trends of near-surface winds for both seasons. There are marked differences between seasons over the tropical western Pacific, but over the tropical Indian Ocean the enhanced northerlies and northwesterlies are present in both seasons. In JJA the increased northerlies over the tropical Indian Ocean and southern Asia represent a weakening of the Asian monsoon, consistent with recent simulations of the effect of South Asian aerosol [*Ramanathan et al.*, 2005]. In DJF, the increased northerlies and northwesterlies represent a strengthening of the reversed flow, which brings the monsoonal rainfall to northern Australia. Note that even though there is less solar radiation over South Asia and the northern Indian Ocean in DJF, the aerosol loading there is much larger in that season, since there is less scavenging by rainfall [e.g., *Ramanathan et al.* 2001]. Our result for DJF differs from that of *Ramanathan et al.* [2005], who found that the South Asian aerosol haze induced a circulation change in DJF that was of the opposite sense to that induced in JJA in their model. This may reflect the different experimental designs used in the two studies and merits further investigation.

[50] It would be desirable to evaluate our modeled trends in atmospheric circulation using a product such as the 50-year NCEP-NCAR reanalysis [*Kalnay et al.*, 1996]. However, serious doubts have been raised about the suitability of the reanalysis for evaluation of circulation changes

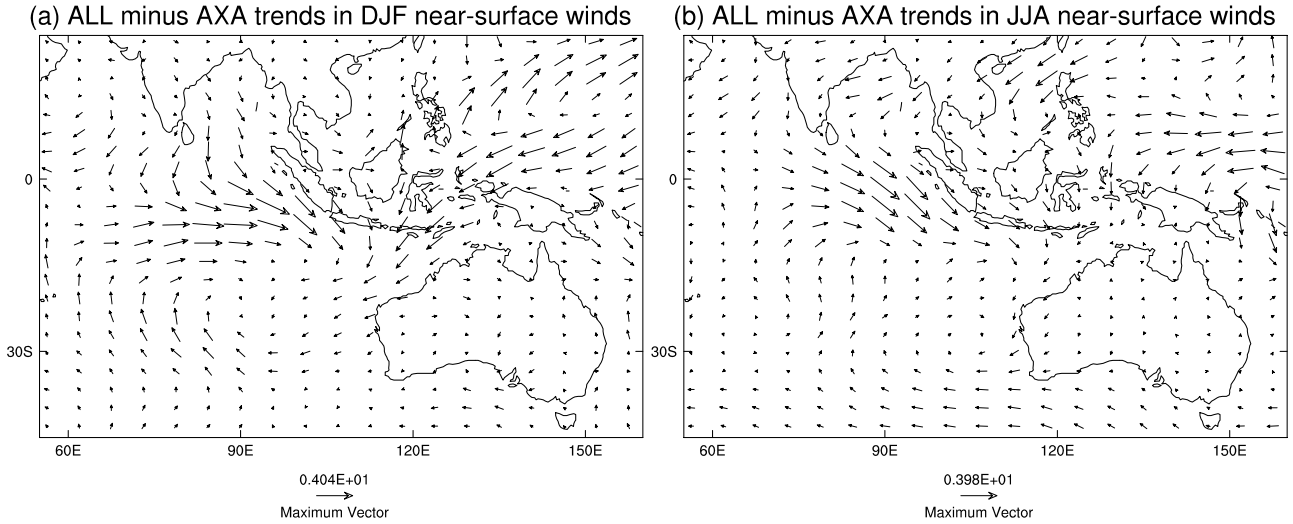

Figure 15. Differences (ALL minus AXA) in ensemble-mean trends in near-surface winds (m/s/century) for (a) DJF and (b) JJA.

in the tropics, due to changes in the observing system and/or data assimilation procedures [*Kinter et al.*, 2004]. We similarly found that apparent trends in the reanalysis were not consistent with circulation changes expected from the observed T_s trends in Figure 11a.

4.2. Oceanic Aspects

[51] The associated oceanic processes due to increasing aerosols may be assessed from differences between the ALL and AXA ensembles (ALL minus AXA). Figures 16a and 16b show the trend differences in surface wind stress and near-surface oceanic currents (averaged over 0 to 240 m depth). Over the southeastern tropical Indian Ocean, the cyclonic wind stress trend pattern (Figure 16a) with westerlies and northwesterlies along the Sumatra-Java coast are conducive to warming of the eastern Indian Ocean through the combined effects of downwelling generated locally along the coast and eastward propagating equatorial downwelling Kelvin waves remotely induced from the central equatorial Indian Ocean. The trend pattern resembles that associated with the negative phase of the Indian Ocean Dipole [*Saji et al.*, 1999]. These processes are reflected in the contrast between trends in the ALL ensemble mean (Figure 12c), in which westerlies and northwesterlies along the Sumatra-Java coast are clearly shown, and in the AXA ensemble mean (Figure 12d), where the absence of aerosol forcing produces opposite trends with southeasterlies promoting cooling off the Sumatra-Java coast.

[52] Over the Pacific sector, the wind stress trend pattern resembles that during a La Niña event, with substantial easterly anomalies in the equatorial Pacific promoting upwelling-induced cooling along the Equator, and a cyclonic wind stress trend pattern over the subtropical and midlatitude southwestern Pacific Ocean (Figure 16a). These wind stress trends induce ocean circulation changes consisting of northward flows along the western boundary into the equatorial Pacific (Figure 16b). Feeding the northward flows are westward currents at latitudes north of New Zealand, contributing to cooling seen in Figure 11c as they advect cool water to lower latitudes from east of New

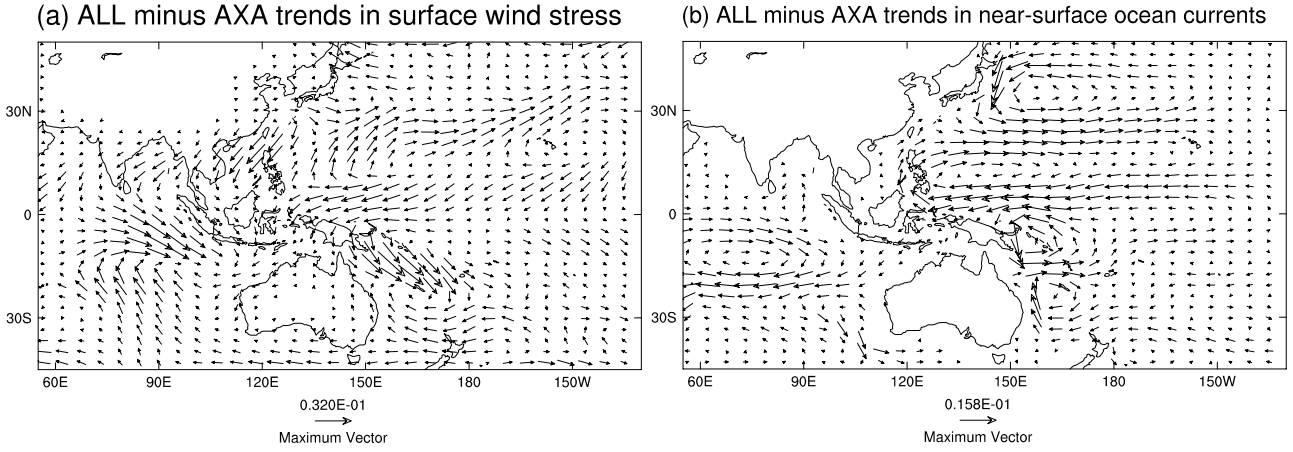

Figure 16. Ensemble-mean differences (ALL minus AXA) in trends of (a) surface wind stress (N/m^2/century) and (b) near-surface ocean currents (m/s/century) for the period 1951–1996.

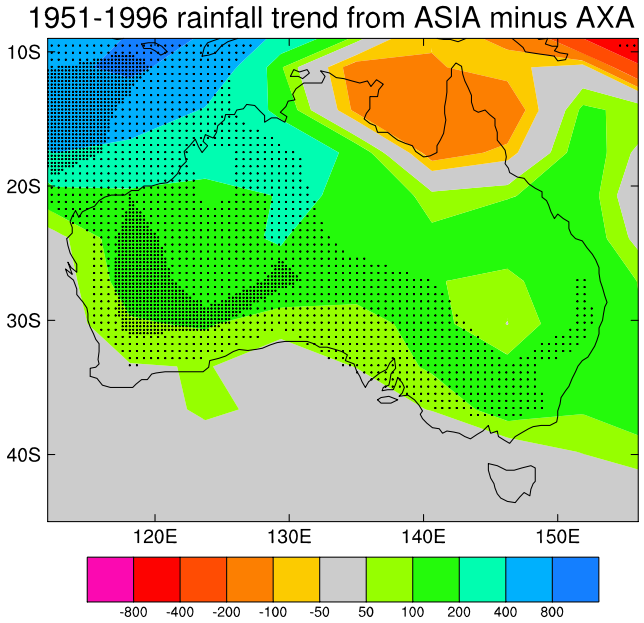

Figure 17. Ensemble-mean differences (ASIA minus AXA) in 1951–1996 annual rainfall trends (mm per century). Light (heavy) stippling shows areas where the trends are significant at 10% (1%).

Zealand. These flows feed a stronger Indonesian Throughflow, contributing to a strengthening of the South Equatorial Current of the Indian Ocean and the modeled Leeuwin Current. The stronger Indonesian Throughflow is another mechanism that contributes to the warming over the eastern Indian Ocean.

[53] In summary, aerosol forcing produces circulation changes of the entire Indo-Pacific system, with a La Niña-like trend pattern, a negative Indian Ocean Dipole-like trend, and a stronger Indonesian Throughflow; the coexistence of these features is consistent with their relationship on interannual timescales [*Meyers*, 1996; *Cai et al.*, 2005b]. This result may have important implications for our understanding of climate change in regions other than Australia and merits further investigation.

5. Isolating the Impact of Asian Aerosols

[54] Since our ALL ensemble included anthropogenic aerosols from all regions, it is valid to ask whether the response of the model over Australia is entirely or predominantly due to aerosols from Asia, as we have claimed. To test this, we performed another eight-member ensemble ("ASIA"), in which only Asian anthropogenic aerosols were included. The setup was identical to that of the ALL ensemble, except that emissions of anthropogenic aerosols and their precursors were held fixed at their 1870 levels outside the rectangular region that we defined as "Asia" in section 2.3. Figure 17 shows the difference (ASIA minus AXA) in ensemble-mean annual rainfall trends over Australia, i.e., the effect of Asian anthropogenic aerosols. The pattern is very similar to that shown in Figure 8d, confirming that the response of the model over Australia is predominantly due to aerosols from Asia.

[55] Another question is whether the shift toward a more La Niña-like pattern of SST change in the ALL ensemble is related to anthropogenic aerosols from Asia or from elsewhere. We recalculated the 1951–1996 SST trends from the ASIA ensemble for the shifted Niño 3.4 and tropical western Pacific boxes, as we did for the other ensembles in section 4.1. In the ASIA ensemble, the difference between the SST trends (eastern box minus western box) is +0.23 K/century. This represents a warming trend that is less El Niño-like than that in the AXA ensemble (+0.68 K/century) but not as La Niña-like as that in the ALL ensemble (−0.02 K/century). This suggests that the more La Niña-like SST trend pattern in the ALL ensemble is partly related to anthropogenic aerosols from regions other than Asia. According to *Cai and Whetton* [2000], the SST trend in the tropical eastern Pacific in the second half of the 20th century is related to the SST trend in the extratropical North Pacific in the first half of the century because the surface waters from the North Pacific take several decades to travel to the tropical Pacific via the deep ocean. To check this, we show in Figure 18 the differences (ALL minus AXA and ASIA minus AXA) in ensemble-mean T_s trends over the North Pacific region during 1901–1950. There is a marked cooling trend of North Pacific SST due to the inclusion of anthropogenic aerosols in the ALL ensemble, which is only weakly present in the ASIA ensemble. This tends to confirm that the mechanism described by *Cai and Whetton* [2000] is present in our simulations and that the more La Niña-like SST trend pattern in the ALL ensemble

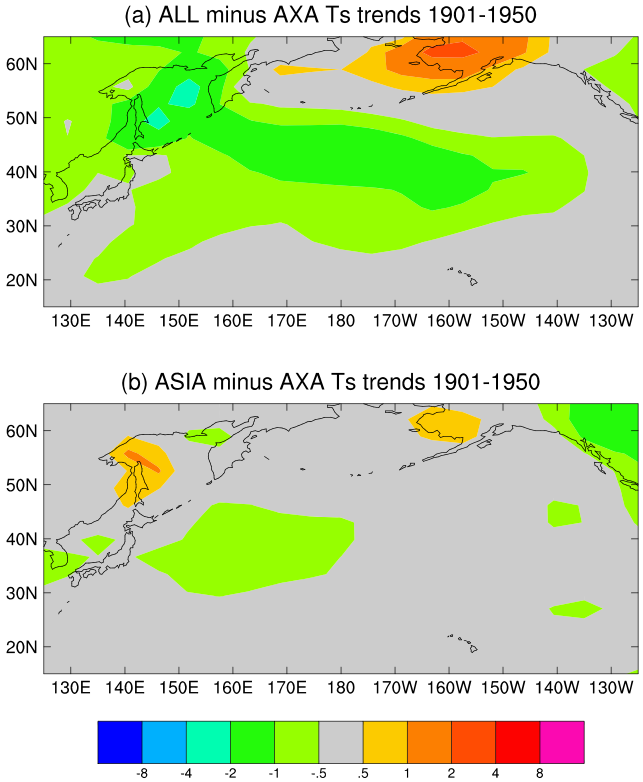

Figure 18. Ensemble-mean differences in 1901–1950 T_s trends (K/century) over the North Pacific region: (a) ALL minus AXA, and (b) ASIA minus AXA.

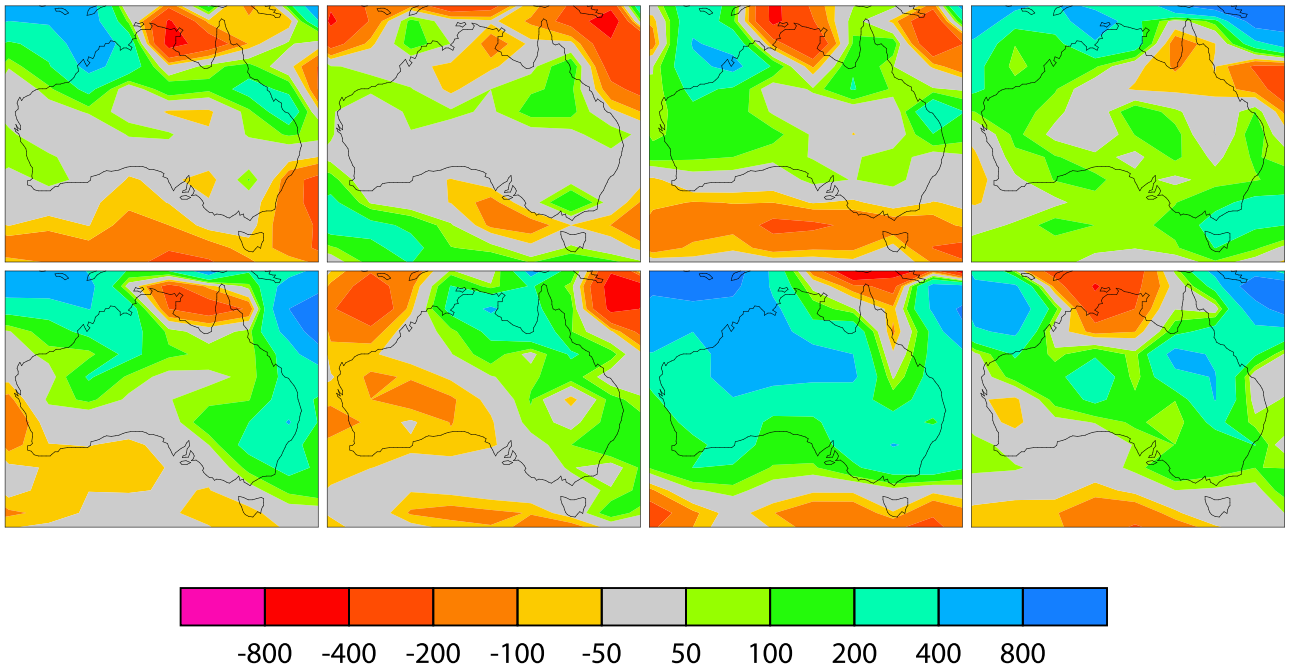

Figure 19. The 1951–1996 annual rainfall trends (mm per century) for the eight runs in the ALL ensemble.

is partly related to anthropogenic aerosols from regions other than Asia.

6. Further Discussion

[56] The ensemble means shown in the preceding figures do not give a sense of the variability between runs, which is substantial. Although our low-resolution model underestimates El Niño-like variability, it does have substantial variability on multidecadal timescales. Figure 19 shows the rainfall trends for the eight members of the ALL ensemble. All members have a positive trend in annual rainfall when averaged over Australia, ranging from 24 mm/century to 280 mm/century, but the patterns differ strongly in some of the runs. These results emphasize that natural interdecadal fluctuations have probably contributed to the observed trends in the Australian hydrological cycle, even though the runs with anthropogenic aerosols show a stronger propensity for increasing rainfall and cloudiness. It is possible that our low-resolution simulations overestimate interdecadal rainfall variability over Australia, which would tend to exaggerate the differences among the panels of Figure 19. We suspect this to be the case because when we computed the power spectrum of global-mean near-surface temperature and compared it to the observed power spectrum (not shown), the model had too little variability on ENSO-like timescales but too much variability on 10 to 30-year timescales. This is an important topic for further research.

[57] Our hypothesis (regarding attribution of the rainfall trends over northwestern and central Australia) would be more convincing if the inclusion of anthropogenic aerosols had improved the agreement with observed rainfall trends over the whole of Australia. In fact, the annual rainfall trends in the ALL ensemble show worse agreement with observed trends over much of eastern and southern Australia (Figure 8). The rainfall trends for eastern Australia are difficult to interpret, given that there are currently no detailed studies, and insufficient evidence to clearly distinguish the trends from natural variability. If the observed rainfall decreases over eastern Australia do reflect a shift toward more El Niño-like conditions in the late 20th century, then a possible interpretation of our result is that the extent to which anthropogenic aerosols make the Pacific Ocean warming pattern more La Niña-like is overestimated by our model. Over southern Australia, a likely explanation for the less realistic rainfall trends shown by the ALL ensemble is that, because the midlatitude frontal systems are located too far south in the model, southern Australia responds as a part of the subtropical regime, and the greenhouse-warming "signature" of a southward shift of the midlatitude frontal systems is displaced to the south. It is interesting that the changes in rainfall trends due to inclusion of Asian anthropogenic aerosols (Figure 17) are similar to those due to all anthropogenic aerosols (Figure 8d) over mainland Australia, but Asian aerosols do not induce the increasing rainfall trends to the south of the continent that are seen in Figure 8d. A possible interpretation of this result is that in the ALL ensemble, aerosol forcing substantially offsets the overall warming due to greenhouse gases, so the greenhouse-induced southward shift of the midlatitude frontal systems is weakened. In the ASIA ensemble, the global-mean warming is only slightly reduced relative to that in the AXA ensemble (not shown), so this weakening of the southward shift of the midlatitude frontal systems is much less evident. However, the regional dynamic response (induced by the meridional T_s gradient in the Australasian region) is still present in the ASIA ensemble.

[58] Aside from the reservations expressed in the previous paragraph, there are several other caveats regarding our results. One limitation is the coarse resolution of the model, which also necessitated the use of an older version of the Cox-Bryan ocean model than that used in our high-resolution (spectral T63) GCM. This choice was largely due to computational constraints, and it would be desirable to repeat these experiments with our T63 model, which has several advantages (including a better simulation of El Niño-like variability). It is also essential to check whether our results can be reproduced by other GCMs. As discussed in section 2.4.2, many aspects of the aerosol treatment are highly simplified, and some aerosol-related climate feedbacks are omitted from the model. Also, it is possible that the model's underestimate of AOD over many regions may cause the contribution to Australian climatic trends from Asian anthropogenic aerosols to be overestimated, or the contribution from East Asia to be overestimated relative to that from South Asia. (Note that we have not attempted to break down the effects of Asian aerosols into contributions from different parts of Asia.) Many other aspects of the model are also uncertain, and (for example) the response of the GCM to spatially inhomogeneous forcing is likely to be sensitive to the treatment of moist atmospheric processes such as clouds and convection. The HadCRUT2 near-surface temperature observations provide some support for our simulations, but we were unable to draw any conclusions regarding our simulated SLP trends, due to large differences among the historical SLP data sets. Also, the very different rainfall trend patterns shown by the individual members of the ALL ensemble (Figure 19) are a reminder of the difficulty of attributing cause and effect in a deterministic manner.

7. Conclusions

[59] The most robust conclusion from this study is that forcing from anthropogenic aerosols should not be neglected in future modeling of Australian climate change. Our results also suggest the hypothesis that Asian anthropogenic aerosols have substantially affected the hydrological cycle in the Australian region, by altering the meridional temperature gradient between Asia and northern Australia. These aerosols are a possible cause of the increasing Australian rainfall trend centered over the northwestern part of the continent. Whereas anthropogenic aerosols may suppress the hydrological cycle over southern Asia, the compensating circulation changes may enhance it over much of Australia. The effect of including anthropogenic aerosols in the model resembles a negative Indian Ocean Dipole-like trend pattern, with relatively warmer SSTs in the southeastern tropical Indian Ocean than in the northwestern tropical Indian Ocean. This pattern has been associated with increased rainfall and convection over Australia (though we note that previous research has mostly linked it to increased Australian winter rainfall, whereas the increasing rainfall trend over northwestern Australia is primarily a summertime phenomenon). Anthropogenic aerosols also make the simulated pattern of SST change in the tropical Pacific more like La Niña, since they induce a cooling of the surface waters in the extratropical North Pacific, which are then transported to the tropics several decades later via the deep ocean. This response of our model was partly due to aerosols from regions other than Asia. It raises the intriguing possibility that just as anthropogenic aerosols are postulated to have "protected" the North Atlantic thermohaline circulation from a greenhouse-induced weakening [*Delworth and Dixon*, 2006], they may have offset some of the greenhouse-induced pattern of El Niño-like SST change in the Pacific. This could have important implications for our understanding of climate change in Australia and in other regions that are affected by ENSO. While we have focused on Australia in this paper, our results suggest that aerosol forcing may have influenced atmospheric circulation and rainfall over the Maritime Continent and the wider Indo-Pacific region, and this would be an interesting topic for further study.

[60] The above conclusions are all subject to the caveat that many aspects of our model are uncertain or highly simplified, as discussed in section 2.4. This highlights the need for more research to better understand the properties of aerosols and their direct and indirect effects on climate.

[61] If our results are correct, then future long-term rainfall trends over northwestern and central Australia are likely to be related to trends in Asian aerosol levels. Although global emissions of aerosols and aerosol precursors are generally expected to decline by 2030 [*Streets et al.*, 2004], the future of Asian emissions is more uncertain, due to rapid economic growth in that region. For example, *Streets et al.* [2004] project an increase of BC emissions in 2030 from South Asia and Southeast Asia (but not East Asia) in some of the IPCC scenarios. By 2050, they expect Asian emissions of BC and POM to be lower than in 1996, and the same is true for SO_2 in most of the scenarios considered by *Nakicenovic et al.* [2000]. If recent rainfall decreases in eastern and southwestern Australia (Figure 8a) are related to increased levels of greenhouse gases, as suggested by some studies, then decreasing Asian aerosol levels may eventually augment a long-term trend of decreasing rainfall over Australia. However, other possible causes of existing rainfall trends (including land clearing and natural variability) have been proposed, and these suggest very different future scenarios for Australian rainfall. It is therefore an urgent priority to resolve these uncertainties, or our ability to predict the magnitude and sign of Australian regional climate change will be severely limited.

[62] **Acknowledgments.** This work was funded in part by the Australian Greenhouse Office. GDF acknowledges support from the Gary Comer Award. We thank Ian Smith, Penny Whetton, Dörte Jakob, and Michael Hobbins for their comments on the manuscript and Tim Cowan for help with computing. We are grateful to Stefan Kinne, who provided the climatologies of aerosol optical depth and single-scattering albedo and also commented on the manuscript. NOAA Extended Reconstructed SLP data were provided by the NOAA/OAR/ESRL PSD, Boulder, Colorado, USA, from their Web site at http://www.cdc.noaa.gov/.

References

Adams, P. J., J. H. Seinfeld, D. M. Koch, L. Mickley, and D. Jacob (2001), General circulation model assessment of direct radiative forcing by the sulfate-nitrate-ammonium-water inorganic aerosol system, *J. Geophys. Res.*, *106*, 1097–1111.

Albrecht, B. A. (1989), Aerosols, cloud microphysics, and fractional cloudiness, *Science*, *245*, 1227–1230.

Allan, R. J., and T. J. Ansell (2006), A new globally complete monthly historical mean sea level pressure data set (HadSLP2): 1850–2004, *J. Clim.*, *19*, 5816–5842.

Andreae, M. O., D. Rosenfeld, P. Artaxo, A. A. Costa, G. P. Frank, K. M. Longo, and M. A. F. Silva-Dias (2004), Smoking rain clouds over the Amazon, *Science*, *303*, 1337–1342.

Arblaster, J. M., and G. A. Meehl (2006), Contributions of external forcings to Southern Annular Mode trends, *J. Clim.*, *19*, 2896–2905.

Ashok, K., Z. Guan, and T. Yamagata (2003), Influence of the Indian Ocean Dipole on the Australian winter rainfall, *Geophys. Res. Lett.*, *30*(15), 1821, doi:10.1029/2003GL017926.

Bellouin, N., O. Boucher, D. Tanre, and O. Dubovik (2003), Aerosol absorption over the clear-sky oceans deduced from POLDER-1 and AERONET observations, *Geophys. Res. Lett.*, *30*(14), 1748, doi:10.1029/2003GL017121.

Boucher, O., and U. Lohmann (1995), The sulfate-CCN-cloud albedo effect. A sensitivity study with two general circulation models, *Tellus, Ser. B*, *47*, 281–300.

Cai, W., and P. H. Whetton (2000), Evidence for a time-varying pattern of greenhouse warming in the Pacific Ocean, *Geophys. Res. Lett.*, *27*, 2577–2580.

Cai, W., P. H. Whetton, and D. J. Karoly (2003a), The response of the Antarctic oscillation to increasing and stabilized atmospheric CO_2, *J. Clim.*, *16*, 1525–1538.

Cai, W., M. A. Collier, H. B. Gordon, and L. J. Waterman (2003b), Strong ENSO variability and a Super-ENSO pair in the CSIRO Mark 3 coupled climate model, *Mon. Weather Rev.*, *31*, 1189–1210.

Cai, W., H. H. Hendon, and G. Meyers (2005a), Indian Ocean Dipolelike Variability in the CSIRO Mark 3 Coupled Climate Model., *J. Clim.*, *18*, 1449–1468.

Cai, W., G. Meyers, and G. Shi (2005b), Transmission of ENSO signal to the Indian Ocean, *Geophys. Res. Lett.*, *32*, L05616, doi:10.1029/2004GL021736.

Cai, W., G. Shi, and Y. Li (2005c), Multidecadal fluctuations of winter rainfall over southwest Western Australia simulated in the CSIRO Mark 3 coupled model, *Geophys. Res. Lett.*, *32*, L12701, doi:10.1029/2005GL022712.

Charlson, R. J., J. E. Lovelock, M. O. Andreae, and S. G. Warren (1987), Oceanic phytoplankton, atmospheric sulphur, cloud albedo and climate, *Nature*, *326*, 655–661.

Chou, M.-D., and K.-T. Lee (2005), A parameterization of the effective layer emission for infrared radiation calculations, *J. Atmos. Sci.*, *62*, 531–541.

Chou, M.-D., M. J. Suarez, X.-Z. Liang, and M. M.-H. Yan (2001), A thermal infrared radiation parameterization for atmospheric studies, *Tech. Memo. 104606*, vol. 19, 56 pp., NASA, Washington, D. C.

Clarke, G. K. C., H. L. Treut, R. S. Lindzen, V. P. Meleshko, R. K. Mugara, T. N. Palmer, R. T. Pierrehumbert, P. J. Sellers, and J. W. K. E. Trenberth (2001), Physical climate processes and feedbacks, in *Climate Change 2001: The Scientific Basis. Contribution of Working Group I to the Third Assessment Report of the Intergovernmental Panel on Climate Change (IPCC)*, edited by J. T. Houghton et al., pp. 417–470, Cambridge Univ. Press, New York.

Cooke, W. F., C. Liousse, H. Cachier, and J. Feichter (1999), Construction of a $1° \times 1°$ fossil fuel emission data set for carbonaceous aerosol and implementation and radiative impact in the ECHAM4 model, *J. Geophys. Res.*, *104*, 22,137–22,162.

Cox, M. D. (1984), A primitive equation, three-dimensional model of the ocean, *Tech. Report 1*, 143 pp., Geophys. Fluid Dyn. Lab. Ocean Group, Princeton, N. J.

Cubasch, U., G. A. Meehl, G. J. Boer, R. J. Stouffer, M. Dix, A. Noda, C. A. Senior, S. Raper, and K. S. Yap (2001), Projections of future climate change, in *Climate Change 2001: The Scientific Basis. Contribution of Working Group I to the Third Assessment Report of the Intergovernmental Panel on Climate Change*, edited by J. T. Houghton et al., pp. 525–582, Cambridge Univ. Press, New York.

Dai, A., A. D. Del Genio, and I. Y. Fung (1997), Clouds, precipitation and temperature range, *Nature*, *386*, 665–666.

d'Almeida, G. A., P. Koepke, and E. P. Shettle (1991), *Atmospheric Aerosols: Global Climatology and Radiative Characteristics*, 561 pp., A. Deepak, Hampton, Va.

Della-Marta, P. M., D. A. Collins, and K. Braganza (2004), Updating Australia's high-quality annual temperature dataset, *Aust. Meteorol. Mag.*, *53*, 75–93.

Delworth, T. L., and K. W. Dixon (2006), Have anthropogenic aerosols delayed a greenhouse gas-induced weakening of the North Atlantic thermohaline circulation?, *Geophys. Res. Lett.*, *33*, L02606, doi:10.1029/2005GL024980.

de Reus, M., F. Dentener, A. Thomas, S. Borrmann, J. Strm, and J. Lelieveld (2000), Airborne observations of dust aerosol over the North Atlantic Ocean during ACE 2: Indications for heterogeneous ozone destruction, *J. Geophys. Res.*, *105*, 15,263–15,275.

Feichter, J., E. Kjellström, H. Rodhe, F. Dentener, J. Lelieveld, and G.-J. Roelofs (1996), Simulation of the tropospheric sulfur cycle in a global climate model, *Atmos. Environ.*, *30*, 1693–1707.

Feichter, J., E. Roeckner, U. Lohmann, and B. Liepert (2004), Nonlinear aspects of the climate response to greenhouse gas and aerosol forcing, *J. Clim.*, *17*, 2384–2398.

Flato, G. M., and W. Hibler III (1990), On a simple sea ice dynamics model for climate studies, *Adv. Geophys.*, *14*, 72–77.

Francis, P. N., A. Jones, R. W. Saunders, K. P. Shine, A. Slingo, and Z. Sun (1994), An observational and theoretical study of the radiative properties of cirrus: Some results from ICE'89, *Q. J. R. Meteorol. Soc.*, *120*, 809–848.

Gabric, A. J., R. Cropp, A. C. Hirst, and H. Marchant (2003), The sensitivity of dimethyl sulfide production to simulated climate change in the Eastern Antarctic Southern Ocean, *Tellus, Ser. B*, *55*, 966–981.

Gent, P. R., J. Willebrand, T. J. McDougall, and J. C. McWilliams (1995), Parameterizing eddy-induced tracer transports in ocean circulation models, *J. Phys. Oceanogr.*, *25*, 463–474.

Gerber, H. E. (1985), Relative-humidity parameterization of the Navy Aerosol Model (nam), *NRL Rep. 8956*, 13 pp., Naval Res. Lab., Washington, D. C.

Ghan, S., N. Laulainen, R. Easter, R. Wagener, S. Nemesure, E. Chapman, Y. Zhang, and R. Leung (2001), Evaluation of aerosol direct radiative forcing in MIRAGE, *J. Geophys. Res.*, *106*, 5295–5316.

Gillett, N. P., R. J. Allan, and T. J. Ansell (2005), Detection of external influence on sea level pressure with a multi-model ensemble, *Geophys. Res. Lett.*, *32*, L19714, doi:10.1029/2005GL023640.

Ginoux, P., J. M. Prospero, O. Torres, and M. Chin (2004), Long-term simulation of global dust distribution with the GOCART model: Correlation with North Atlantic Oscillation, *Environ. Model. Software*, *19*, 113–128.

Gordon, H. B., and S. P. O'Farrell (1997), Transient climate change in the CSIRO coupled model with dynamic sea ice, *Mon. Weather Rev.*, *125*, 875–907.

Gordon, H. B., et al. (2002), The CSIRO Mk3 Climate System Model, *Tech. Pap. 60*, 134 pp., CSIRO Atmos. Res., Aspendale, Victoria, Australia. (Available online at http://www.cmar.csiro.au/e-print/open/gordon_2002a.pdf.)

Graf, H., J. Feichter, and B. Langmann (1997), Volcanic sulfur emissions: Estimates of source strength and its contribution to the global sulfate distribution, *J. Geophys. Res.*, *102*, 10,727–10,738.

Grant, K. E., and A. S. Grossman (1998), Description of a solar radiative transfer model for use in LLNL climate and atmospheric chemistry studies, *Rep. UCRL-ID-129949*, 17 pp., Lawrence Livermore Natl. Lab., Livermore, Calif. (Available online at http://www.llnl.gov/tid/lof/documents/pdf/233048.pdf.)

Grant, K. E., C. C. Chuang, A. S. Grossman, and J. E. Penner (1999), Modeling the spectral optical properties of ammonium sulfate and biomass burning aerosols: parameterization of relative humidity effects and model results, *Atmos. Environ.*, *33*, 2603–2620.

Gregory, D., and P. R. Rowntree (1990), A mass flux convection scheme with representation of cloud ensemble characteristics and stability-dependent closure, *Mon. Weather Rev.*, *118*, 1483–1506.

Guenther, A., et al. (1995), A global model of natural volatile organic compound emissions, *J. Geophys. Res.*, *100*, 8873–8892.

Hansen, J., and L. Nazarenko (2004), Soot climate forcing via snow and ice albedos, *Proc. Natl. Acad. Sci.*, *101*, 423–428, doi:10.1073/pnas.2237157100.

Hansen, J., M. Sato, and R. Ruedy (1995), Long-term changes of the diurnal temperature cycle: Implications about mechanisms of global climate change, *Atmos. Res.*, *37*, 175–209.

Hansen, J., et al. (2002), Climate forcings in Goddard Institute for Space Studies SI2000 simulations, *J. Geophys. Res.*, *107*(D18), 4347, doi:10.1029/2001JD001143.

Hansen, J., et al. (2005), Efficacy of climate forcings, *J. Geophys. Res.*, *110*, D18104, doi:10.1029/2005JD005776.

Hirst, A. C., S. P. O'Farrell, and H. B. Gordon (2000), Comparison of a coupled ocean-atmosphere model with and without oceanic eddy-induced advection. Part I: ocean spinup and control integrations, *J. Clim.*, *13*, 139–163.

Hobbs, P. V., J. S. Reid, R. A. Kotchenruther, R. J. Ferek, and R. Weiss (1997), Direct radiative forcing by smoke from biomass burning, *Science*, *275*, 1776–1778.

Holben, B. N., et al. (2001), An emerging ground-based aerosol climatology: Aerosol optical depth from AERONET, *J. Geophys. Res.*, *106*, 12,067–12,098.

Holtslag, A. A. M., and B. A. Boville (1993), Local versus non-local boundary layer diffusion in a global climate model, *J. Clim.*, *6*, 1825–1842.

Ignatov, A., and N. Nalli (2002), Aerosol retrievals from multi-satellite AVHRR pathfinder (PATMOS) data-set for correcting remotely sensed sea surface temperature, *J. Atmos. Ocean. Tech.*, *19*, 1986–2008.

Ishizaka, Y., and M. Adhikari (2003), Composition of cloud condensation nuclei, *J. Geophys. Res.*, *108*(D4), 4138, doi:10.1029/2002JD002085.
Ito, A., and J. E. Penner (2005), Historical emissions of carbonaceous aerosols from biomass and fossil fuel burning for the period 1870–2000, *Global Biogeochem. Cycles*, *19*, GB2028, doi:10.1029/2004GB002374.
Jacobson, M. Z. (2001), Strong radiative heating due to the mixing state of black carbon in atmospheric aerosols, *Nature*, *409*, 695–697.
Jacobson, M. Z. (2004), The short-term cooling but long-term global warming due to biomass burning, *J. Clim.*, *17*, 2909–2926.
Jones, A., D. L. Roberts, M. J. Woodage, and C. E. Johnson (2001), Indirect sulphate aerosol forcing in a climate model with an interactive sulfur cycle, *J. Geophys. Res.*, *106*, 20,293–20,310.
Jones, P. A., and A. Henderson-Sellers (1992), Historical records of cloudiness and sunshine in Australia, *J. Clim.*, *5*, 260–267.
Jones, P. D., and A. Moberg (2003), Hemispheric and large-scale surface air temperature variations: An extensive revision and an update to 2001, *J. Clim.*, *16*, 206–223.
Kalnay, E., et al. (1996), The NCEP/NCAR 40-year reanalysis project, *Bull. Am. Meteorol. Soc.*, *77*, 437–471.
Kanakidou, M., et al. (2005), Organic aerosol and global climate modelling: a review, *Atmos. Chem. Phys.*, *5*, 1053–1123.
Karoly, D. J., and K. Braganza (2005), Attribution of recent temperature changes in the Australian region, *J. Clim.*, *18*, 457–464.
Kaufman, Y. J., D. Tanré, L. A. Remer, E. F. Vermote, A. Chu, and B. N. Holben (1997), Operational remote sensing of tropospheric aerosol over land from EOS moderate resolution imaging spectroradiometer, *J. Geophys. Res.*, *102*, 17,051–17,068.
Kaufman, Y. J., O. Boucher, D. Tanré, M. Chin, L. A. Remer, and T. Takemura (2005), Aerosol anthropogenic component estimated from satellite data, *Geophys. Res. Lett.*, *32*, L17804, doi:10.1029/2005GL023125.
Kettle, A. J., and M. O. Andreae (2000), Flux of dimethylsulfide from the oceans: A comparison of updated data sets and flux models, *J. Geophys. Res.*, *105*, 26,793–26,808.
Kettle, A. J., et al. (1999), A global database of sea surface dimethylsulfide (DMS) measurements and a procedure to predict sea surface DMS as a function of latitude, longitude and month, *Global Biogeochem. Cycles*, *13*, 399–444.
Khain, A., and A. Pokrovsky (2004), Simulation of effects of atmospheric aerosols on deep turbulent convective clouds using a spectral microphysics mixed-phase cumulus cloud model. part ii: Sensitivity study, *J. Atmos. Sci.*, *61*, 2983–3001.
Khairoutdinov, M. F., and D. A. Randall (2001), A cloud resolving model as a cloud parameterization in the NCAR Community Climate System Model: Preliminary results, *Geophys. Res. Lett.*, *28*, 3617–3620.
Kiehl, J. T., T. L. Schneider, R. W. Portmann, and S. Solomon (1999), Climate forcing due to tropospheric and stratospheric ozone, *J. Geophys. Res.*, *104*, 31,239–31,254.
Kinne, S., et al. (2006), An AeroCom initial assessment–Optical properties in aerosol component modules of global models, *Atmos. Chem. Phys.*, *6*, 1815–1834.
Kinter, J. L., III, M. J. Fennessy, V. Krishnamurthy, and L. Marx (2004), An evaluation of the apparent interdecadal shift in the tropical divergent circulation in the NCEP NCAR reanalysis, *J. Clim.*, *17*, 349–361.
Knutson, T. R., S. Manabe, and D. Gu (1997), Simulated ENSO in a global coupled ocean-atmosphere model: Multidecadal amplitude modulation and CO_2 sensitivity, *J. Clim.*, *10*, 138–161.
Koren, I., Y. J. Kaufman, L. A. Remer, and J. V. Martins (2004), Measurement of the effect of Amazon smoke on inhibition of cloud formation, *Science*, *303*, 1342–1345.
Kristjánsson, J. E., T. Iversen, A. Kirkevåg, O. Seland, and J. Debernard (2005), Response of the climate system to aerosol direct and indirect forcing: Role of cloud feedbacks, *J. Geophys. Res.*, *110*, D24206, doi:10.1029/2005JD006299.
Lance, S., A. Nenes, and T. A. Rissman (2004), Chemical and dynamical effects on cloud droplet number: Implications for estimates of the aerosol indirect effect, *J. Geophys. Res.*, *109*, D22208, doi:10.1029/2004JD004596.
Lavery, B., G. Joung, and N. Nicholls (1997), An extended high-quality historical rainfall dataset for Australia, *Aust. Meteorol. Mag.*, *46*, 27–38.
Lean, J., and D. Rind (1998), Climate forcing by changing solar radiation, *J. Clim.*, *11*, 3069–3094.
Lewis, E. R., and S. E. Schwartz (Eds.) (2004), *Sea Salt Aerosol Production: Mechanisms, Methods, Measurements, and Models—A Critical Review*, *Geophys. Monogr. Ser.*, vol. 152, 413 pp., AGU, Washington, D. C.
Liepert, B. G., J. Feichter, U. Lohmann, and E. Roeckner (2004), Can aerosols spin down the water cycle in a warmer and moister world?, *Geophys. Res. Lett.*, *31*, L06207, doi:10.1029/2003GL019060.
Liousse, C., J. E. Penner, C. Chuang, J. J. Walton, H. Eddleman, and H. Cachier (1996), A global three-dimensional model study of carbonaceous aerosols, *J. Geophys. Res.*, *101*, 19,411–19,432.
Liu, X., J. E. Penner, and M. Herzog (2005), Global modeling of aerosol dynamics: Model description, evaluation, and interactions between sulfate and nonsulfate aerosols, *J. Geophys. Res.*, *110*, D18206, doi:10.1029/2004JD005674.
Liu, Y. G., and P. H. Daum (2002), Indirect warming effect from dispersion forcing, *Nature*, *419*, 580–581.
Louis, J.-F. (1979), A parametric model of vertical eddy fluxes in the atmosphere, *Boundary Layer Meteorol.*, *17*, 187–202.
Martonchik, J. V., D. J. Diner, R. A. Kahn, T. P. Ackerman, M. E. Verstraete, B. Pinty, and H. R. Gordon (1998), Techniques for the retrieval of aerosol properties over land and ocean using multi-angle imaging, *IEEE Trans. Geosci. Remote Sens.*, *36*, 1212–1227.
McBride, J. L., and N. Nicholls (1983), Seasonal relationships between Australian rainfall and the Southern Oscillation, *Mon. Weather Rev.*, *111*, 1998–2004.
McGregor, J. L. (1993), Economical determination of departure points for semi-Lagrangian models, *Mon. Weather Rev.*, *121*, 221–230.
Meehl, G. A., and W. M. Washington (1996), El Niño-like climate change in a model with increased atmospheric CO_2 concentrations, *Nature*, *382*, 56–60.
Meehl, G. A., P. R. Gent, J. M. Arblaster, B. L. Otto Bliesner, E. C. Brady, and A. Craig (2001), Factors that affect the amplitude of El Niño in global coupled climate models, *Clim. Dyn.*, *17*, 515–526.
Meneghini, B., I. Simmonds, and I. N. Smith (2007), Association between Australian rainfall and the Southern Annular Mode, *Int. J. Climatol.*, *26*, doi:10.1002/joc.1370, in press.
Menon, S., and L. Rotstayn (2006), The radiative influence of aerosol effects on liquid-phase cumulus and stratiform clouds based on sensitivity studies with two climate models, *Clim. Dyn.*, *27*, 345–356, doi:10.1007/s00382-006-0139-3.
Menon, S., A. D. Del Genio, D. Koch, and G. Tselioudis (2002a), GCM simulations of the aerosol indirect effect: Sensitivity to cloud parameterization and aerosol burden, *J. Atmos. Sci.*, *59*, 692–713.
Menon, S., J. Hansen, L. Nazarenko, and Y. Luo (2002b), Climate effects of black carbon aerosols in China and India, *Science*, *297*, 2250–2253.
Meyers, G. (1996), Variation of Indonesian throughflow and the El Niño-Southern Oscillation, *J. Geophys. Res.*, *101*, 12,255–12,264.
Mitchell, J. F. B., T. C. Johns, J. M. Gregory, and S. F. B. Tett (1995), Climate response to increasing levels of greenhouse gases and sulphate aerosols, *Nature*, *376*, 501–504.
Mitchell, T. D., and P. D. Jones (2005), An improved method of constructing a database of monthly climate observations and associated high-resolution grids, *Int. J. Climatol.*, *25*, 693–712.
Murphy, J. M., and J. F. B. Mitchell (1995), Transient response of the Hadley Centre Coupled Ocean-Atmosphere Model to increasing carbon dioxide. Part II: Spatial and temporal structure of response, *J. Clim.*, *8*, 57–80.
Myhre, G., A. Grini, J. M. Haywood, F. Stordal, B. Chatenet, D. Tanré, J. K. Sundet, and I. S. A. Isaksen (2003), Modeling the radiative impact of mineral dust during the Saharan Dust Experiment (SHADE) campaign, *J. Geophys. Res.*, *108*(18), 8579, doi:10.1029/2002JD002566.
Nakicenovic, N., et al. (2000), *Emissions Scenarios. Special Report of the Intergovernmental Panel on Climate Change*, 570 pp., Cambridge Univ. Press, New York.
Nazarenko, L., and S. Menon (2005), Varying trends in surface energy fluxes and associated climate between 1960–2002 based on transient climate simulations, *Geophys. Res. Lett.*, *32*, L22704, doi:10.1029/2005GL024089.
Nicholls, N. (1989), Sea surface temperatures and Australian winter rainfall, *J. Clim.*, *2*, 965–973.
Nicholls, N. (2003), Continued anomolous warming in Australia, *Geophys. Res. Lett.*, *30*(7), 1370, doi:10.1029/2003GL017037.
Nightingale, P. D., G. Malin, C. S. Law, A. J. Watson, P. S. Liss, M. I. Liddicoat, J. Boutin, and R. C. Upstill-Goddard (2000), In situ evaluation of air-sea gas exchange parameterizations using novel conservative and volatile tracers, *Global Biogeochem. Cycles*, *14*, 373–387.
O'Dowd, C. D., M. H. Smith, I. E. Consterdine, and J. A. Lowe (1997), Marine aerosol, sea-salt, and the marine sulphur cycle: A short review, *Atmos. Environ.*, *31*, 73–80.
O'Farrell, S. P. (1998), Investigation of the dynamic sea ice component of a coupled atmosphere-sea ice general circulation model, *J. Geophys. Res.*, *103*, 15,751–15,782.
Penner, J. E., H. Eddleman, and T. Novakov (1993), Towards the development of a global inventory of black carbon emissions, *Atmos. Environ., Part A*, *27*, 1277–1295.

Penner, J. E. et al. (2001), Aerosols, their direct and indirect effects, in *Climate Change 2001: The Scientific Basis. Contribution of Working Group I to the Third Assessment Report of the Intergovernmental Panel on Climate Change (IPCC)*, edited by J. T. Houghton et al., pp. 289–348, Cambridge Univ. Press, New York.

Philander, S. G. H. (1990), *El Niño, La Niña, and the Southern Oscillation*, *Int. Geophys. Ser.*, vol. 46, 232 pp., Elsevier, New York.

Pincus, R., and S. A. Klein (2000), Unresolved spatial variability and microphysical process rates in large-scale models, *J. Geophys. Res.*, *105*, 27,059–27,065.

Pitman, A. J., G. T. Narisma, R. A. Pielke, and N. J. Holbrook (2004), Impact of land cover change on the climate of southwest Western Australia, *J. Geophys. Res.*, *109*, D18109, doi:10.1029/2003JD004347.

Prospero, J. M., P. Ginoux, O. Torres, S. E. Nicholson, and T. E. Gill (2002), Environmental characterization of global sources of atmospheric soil dust identified with the NIMBUS 7 Total Ozone Mapping Spectrometer (TOMS) absorbing aerosol product, *Rev. Geophys.*, *40*(1), 1002, doi:10.1029/2000RG000095.

Quinn, P. K., V. N. Kapustin, T. S. Bates, and D. S. Covert (1996), Chemical and optical properties of marine boundary layer aerosol particles of the mid-Pacific in relation to sources and meteorological transport, *J. Geophys. Res.*, *101*, 6931–6952.

Ramanathan, V., et al. (2001), The Indian Ocean Experiment: An integrated analysis of the climate forcing and effects of the great Indo-Asian haze, *J. Geophys. Res.*, *106*, 28,371–28,398.

Ramanathan, V., et al. (2005), Atmospheric brown clouds: Impacts on South Asian climate and hydrological cycle, *Proc. Natl. Acad. Sci.*, *102*, 5326–5333.

Randall, D., M. Khairoutdinov, A. Arakawa, and W. Grabowski (2003), Breaking the Cloud Parameterization Deadlock., *Bull. Am. Meteorol. Soc.*, *84*, 1547–1564.

Rayner, N. A., D. E. Parker, E. B. Horton, C. K. Folland, L. V. Alexander, D. P. Rowell, E. C. Kent, and A. Kaplan (2003), Globally complete analyses of sea surface temperature, sea ice and night marine air temperature, *J. Geophys. Res.*, *108*(D14), 4407, doi:10.1029/2002JD002670.

Roderick, M. L., and G. D. Farquhar (2002), The cause of decreased pan evaporation over the past 50 years, *Science*, *298*, 1410–1411.

Roderick, M. L., and G. D. Farquhar (2004), Changes in Australian pan evaporation from 1970 to 2002, *Int. J. Climatol.*, *24*, 1077–1090.

Ropelewski, C. F., and M. S. Halpert (1987), Global and regional scale precipitation associated with El Niño/Southern Oscillation, *Mon. Weather Rev.*, *115*, 1606–1626.

Rosenfeld, D., and I. Lensky (1998), Satellite-based insights into precipitation formation processes in continental and maritime convective clouds, *Bull. Am. Meteorol. Soc.*, *79*, 2457–2476.

Rotstayn, L. D. (1997), A physically based scheme for the treatment of stratiform clouds and precipitation in large-scale models. I: Description and evaluation of the microphysical processes, *Q. J. R. Meteorol. Soc.*, *123*, 1227–1282.

Rotstayn, L. D. (1998), A physically based scheme for the treatment of stratiform clouds and precipitation in large-scale models. II: Comparison of modelled and observed climatological fields, *Q. J. R. Meteorol. Soc.*, *124*, 389–415.

Rotstayn, L. D. (2000), On the "tuning" of autoconversion parameterizations in climate models, *J. Geophys. Res.*, *105*, 15,495–15,507.

Rotstayn, L. D., and Y. Liu (2003), Sensitivity of the first indirect aerosol effect to an increase of cloud droplet spectral dispersion with droplet number concentration, *J. Clim.*, *16*, 3476–3481.

Rotstayn, L. D., and Y. Liu (2005), A smaller global estimate of the second indirect aerosol effect, *Geophys. Res. Lett.*, *32*, L05708, doi:10.1029/2004GL021922.

Rotstayn, L. D., and U. Lohmann (2002a), Tropical rainfall trends and the indirect aerosol effect, *J. Clim.*, *15*, 2103–2116.

Rotstayn, L. D., and U. Lohmann (2002b), Simulation of the tropospheric sulfur cycle in a global model with a physically based cloud scheme, *J. Geophys. Res.*, *107*(D21), 4592, doi:10.1029/2002JD002128.

Rotstayn, L. D., and J. E. Penner (2001), Indirect aerosol forcing, quasiforcing and climate response, *J. Clim.*, *14*, 2960–2975.

Rotstayn, L. D., B. F. Ryan, and J. J. Katzfey (2000a), A scheme for calculation of the liquid fraction in mixed-phase stratiform clouds in large-scale models, *Mon. Weather Rev.*, *128*, 1070–1088.

Rotstayn, L. D., B. F. Ryan, and J. E. Penner (2000b), Precipitation changes in a GCM resulting from the indirect effects of anthropogenic aerosols, *Geophys. Res. Lett.*, *27*, 3045–3048.

Saji, N. H., B. N. Goswami, P. N. Vinayachandran, and T. Yamagata (1999), A dipole mode in the tropical Indian Ocean, *Nature*, *401*, 360–363.

Sato, M., J. E. Hansen, M. P. McCormick, and J. B. Pollack (1993), Stratospheric aerosol optical depth, 1850–1990, *J. Geophys. Res.*, *98*, 22,987–22,994.

Semtner, A. J., Jr. (1976), A model for the thermodynamic growth of sea ice in numerical investigations of climate, *J. Phys. Oceanogr.*, *6*, 379–389.

Shettle, E. P., and R. W. Fenn (1979), Models for the aerosols of the lower atmosphere and the effects of humidity variations on their optical properties, *Tech. Rep. AFGL-TR-79-0214*, Air Force Geophys. Lab., Hanscom Air Force Base, Mass.

Smith, I. N. (2004), An assessment of recent trends in Australian rainfall, *Aust. Meteorol. Mag.*, *53*, 163–173.

Smith, S., R. Andres, E. Conception, and J. Lurz (2004), Historical sulfur dioxide emissions 1850-2000: Methods and results, *JGCRI Res. Rep. PNNL-14537*, 16 pp., Pac. Northwest Natl. Lab., Richland, Wash. (Available at http://www.pnl.gov/main/publications/external/technical_reports/PNNL-14537.pdf.)

Smith, S. J., H. Pitcher, and T. M. L. Wigley (2001), Global and regional anthropogenic sulfur dioxide emissions, *Global Planet. Change*, *29*, 99–119.

Smith, T. M., and R. W. Reynolds (2004), Reconstruction of monthly mean oceanic sea level pressure based on COADS and station data (1854–1997), *J. Atmos. Ocean Technol.*, *21*, 1272–1282.

Spiro, P. A., D. J. Jacob, and J. A. Logan (1992), Global inventory of sulfur emissions with $1° \times 1°$ resolution, *J. Geophys. Res.*, *97*, 6023–6036.

Stanhill, G., and S. Cohen (2001), Global dimming: A review of the evidence for a widespread and significant reduction in global radiation with discussion of its probable causes and possible agricultural consequences, *Agric. For. Meteorol.*, *107*, 255–278.

Streets, D. G., T. C. Bond, T. Lee, and C. Jang (2004), On the future of carbonaceous aerosol emissions, *J. Geophys. Res.*, *109*, D24212, doi:10.1029/2004JD004902.

Takemura, T., T. Nozawa, S. Emori, T. Y. Nakajima, and T. Nakajima (2005), Simulation of climate response to aerosol direct and indirect effects with aerosol transport-radiation model, *J. Geophys. Res.*, *110*, D02202, doi:10.1029/2004JD005029.

Tanré, D., Y. J. Kaufman, M. Herman, and S. Mattoo (1997), Remote sensing of aerosol properties over oceans using the MODIS/EOS spectral radiances, *J. Geophys. Res.*, *102*, 16,971–16,988.

Textor, C., et al. (2006), Analysis and quantification of the diversities of aerosol life cycles within AeroCom, *Atmos. Chem. Phys.*, *6*, 1777–1813.

Thompson, D. W. J., and S. Solomon (2002), Interpretation of recent Southern Hemisphere climate change, *Science*, *296*, 895–899, doi:10.1126/science.1069270.

Timbal, B., J. M. Arblaster, and S. Power (2006), Attribution of the late-twentieth-century rainfall decline in Southwest Australia, *J. Clim.*, *19*, 2046–2062.

Toon, O. B., J. B. Pollack, and B. N. Khare (1976), The optical constants of several atmospheric aerosol species: ammonium sulfate, aluminum oxide, and sodium chloride, *J. Geophys. Res.*, *81*, 5733–5748.

Twitty, J. T., and J. A. Weinman (1971), Radiative properties of carbonaceous aerosols, *J. Appl. Meteorol.*, *10*, 725–731.

Twomey, S. (1977), The influence of pollution on the shortwave albedo of clouds, *J. Atmos. Sci.*, *34*, 1149–1152.

Uppala, S. M., et al. (2005), The ERA-40 re-analysis, *Q. J. R. Meteorol. Soc.*, *131*, 2961–3012.

Van Leer, B. (1977), Towards the ultimate conservative difference scheme. V. A new approach to numerical convection, *J. Comput. Phys.*, *23*, 276–299.

Wardle, R., and I. N. Smith (2004), Modeled response of the Australian monsoon to changes in land surface temperatures, *Geophys. Res. Lett.*, *31*, L16205, doi:10.1029/2004GL020157.

Warren, S. G. (1984), Optical constants of ice from the ultraviolet to the microwave, *Appl. Opt.*, *23*, 1206–1225.

Webster, P. J., and J. Fasullo (2003), Monsoon: Dynamical theory, in *Encyclopedia of Atmospheric Sciences*, edited by J. Holton, J. A. Curry, and J. A. Pyle, pp. 1370–1386, Elsevier, New York.

Whetton, P. H., M. H. England, S. P. O'Farrell, I. G. Watterson, and A. B. Pittock (1996), Global comparison of the regional rainfall results of enhanced greenhouse coupled and mixed layer ocean experiments: Implications for climate change scenario development, *Clim. Change*, *33*, 497–519.

Whetton, P. H., J. J. Katzfey, K. J. Hennessy, X. Wu, J. L. McGregor, and K. Nguyen (2001), Developing scenarios of climate change for southeastern Australia: an example using regional climate model output, *Clim. Res.*, *16*, 181–201.

Wild, M., et al. (2005), From dimming to brightening: Decadal changes in solar radiation at Earth's surface, *Science*, *308*, 847–850.

Williams, K. D., A. Jones, D. L. Roberts, C. A. Senior, and M. J. Woodage (2001), The response of the climate system to the indirect effects of anthropogenic sulfate aerosol, *Clim. Dyn.*, *17*, 845–856.

Yin, J. H. (2005), A consistent poleward shift of the storm tracks in simulations of 21st century climate, *Geophys. Res. Lett.*, *32*, L18701, doi:10.1029/2005GL023684.

Yin, Y., S. Wurzler, Z. Levin, and T. G. Reisin (2002), Interactions of mineral dust particles and clouds: Effects on precipitation and cloud optical properties, *J. Geophys. Res.*, *107*(D23), 4724, doi:10.1029/2001JD001544.

Yu, H., R. E. Dickinson, M. Chin, Y. J. Kaufman, M. Zhou, L. Zhou, Y. Tian, O. Dubovik, and B. N. Holben (2004), Direct radiative effect of aerosols as determined from a combination of MODIS retrievals and GOCART simulations, *J. Geophys. Res.*, *109*, D03206, doi:10.1029/2003JD003914.

Yu, H., et al. (2006), A review of measurement-based assessments of the aerosol direct radiative effect and forcing, *Atmos. Chem. Phys.*, *6*, 613–666.

Zhang, J., and S. A. Christopher (2003), Longwave radiative forcing of Saharan dust aerosols estimated from MODIS, MISR, and CERES observations on Terra, *Geophys. Res. Lett.*, *30*(23), 2188, doi:10.1029/2003GL018479.

W. Cai, M. R. Dix, and L. D. Rotstayn, Marine and Atmospheric Research, CSIRO, Private Bag 1, Aspendale, Victoria, 3195, Australia. (leon.rotstayn@csiro.au)

G. D. Farquhar and M. L. Roderick, CRC for Greenhouse Accounting, Research School of Biological Sciences, Australian National University, GPO Box 475, Canberra, ACT, 2601, Australia.

Y. Feng, M. Herzog, A. Ito, J. E. Penner, and M. Wang, Department of Atmospheric, Oceanic, and Space Sciences, University of Michigan, 2455 Hayward, Ann Arbor, MI 48109-2143, USA.

P. Ginoux, Geophysical Fluid Dynamics Laboratory, NOAA, Forrestal Campus, P. O. Box 308, Princeton, NJ 08542-0308, USA.